Received: 21 June 2020 | Revised: 2 April 2021 | Accepted: 4 May 2021

DOI: 10.1111/jmg.12624

ORIGINAL ARTICLE

Journal of METAMORPHIC GEOLOGY WILEY

Bulk inclusion micro-zircon U–Pb geochronology: A new tool to date low-grade metamorphism

M. Sophie Hollinetz[1] | **David A. Schneider**[2] | **Christopher R. M. McFarlane**[3] | **Benjamin Huet**[4] | **Gerd Rantitsch**[5] | **Bernhard Grasemann**[1]

[1]Department of Geology, University of Vienna, Vienna, Austria

[2]Department of Earth and Environmental Sciences, University of Ottawa, Ottawa, ON, Canada

[3]Department of Earth Sciences, University of New Brunswick, Fredericton, Canada

[4]Department of Hard Rock Geology, Geological Survey of Austria, Vienna, Austria

[5]Department of Applied Geosciences and Geophysics, University of Leoben, Leoben, Austria

Correspondence
M. Sophie Hollinetz, Department of Geology, University of Vienna, Althanstraße 14, A-1090, Vienna, Austria.
Email: marianne.sophie.hollinetz@univie.ac.at

Funding information
Natural Sciences and Engineering Research Council of Canada; Universität Wien, Grant/Award Number: uni:docs fellowship 2018

Handling Editor: Simon Harley

Abstract

Dating low-grade metamorphism is challenging since such rocks commonly lack suitable target minerals for acquiring pressure–temperature–time–deformation (*P–T–t–d*) data. Herein a new geochronological method termed 'bulk inclusion dating' is applied to a chloritoid-bearing schist from the Staufen-Höllengebirge Nappe (SHN, Austroalpine Unit, Eastern Alps, Austria) for which Cretaceous metamorphism is imprecisely constrained. Thermodynamic modelling of the phase relations and mineral chemistry predicts the stability of the equilibrium assemblage in a *P–T* field between 450–490℃ and 0.5–0.7 GPa, which agrees with peak temperature constraints ~490℃ derived from Raman spectroscopy of carbonaceous material. Chemical zoning of, and the zonation of inclusions within, chloritoid confirm porphyroblast growth at these conditions. High-resolution imaging reveals thousands of minute (length: 0.1–3 μm), euhedral micro-zircon crystals included in chloritoid porphyroblasts and in the matrix. The morphological and microstructural characteristics of micro-zircon as well as the crystal size distributions indicate that it nucleated and grew at greenschist facies conditions most likely from a Zr-saturated fluid. In situ laser ablation inductively coupled plasma mass spectroscopy bulk inclusion dating of metamorphic zircon in the chloritoid rim using a laser spot diameter of 120 μm yields a U–Pb age of 116.7 ± 9.1 Ma (MSWD: 1.5, *n*: 79). We interpret zircon precipitation and progressive coarsening coeval with chloritoid growth during prograde metamorphism and thus link the age to the late prograde part of the *P–T* evolution. The contribution of other U-bearing phases (apatite, epidote, rutile) does not significantly disturb the U–Pb age. The data provide clear evidence for Early Cretaceous metamorphism in the SHN and indicates that metamorphism started at least 20 m.y. before the formation of eclogites in the Austroalpine Unit. The method introduced here allows integration between metamorphic conditions and age constraints in low-grade metamorphic rocks and opens up new potential applications in petrochronology.

KEYWORDS

chloritoid, low-grade metamorphism, Thermodynamic modelling, U–Pb geochronology, zircon

1 | INTRODUCTION

Deciphering the petrologic evolution of low-grade metamorphic rocks is essential for a comprehensive understanding of the burial and exhumation processes during orogeny. Linking pressure (*P*), temperature (*T*), age (*t*), and deformation (*d*) data is comparatively straightforward in high-grade metamorphic rocks where some of the rock-forming minerals that can be directly related to *P–T* conditions can also be dated (e.g. Herwartz et al., 2011; Thöni et al., 2008). Low-grade metamorphism and deformation, on the other hand, is commonly dated with white mica geochronology, but linking white mica ages to metamorphic events is sometimes ambiguous due to the complex response of the Rb–Sr and K–Ar isotopic systems to a variety of phenomena (e.g. Cossette et al., 2015; Eberlei et al., 2015; Kula et al., 2010). Certain studies have documented the growth of U–Th-rich phases (e.g. zircon, REE-phosphates, epidote) during low-grade metamorphism (e.g. Dempster et al., 2004; Janots et al., 2006, 2008; Rasmussen, 2005). In situ U–Th–Pb dating of these phases has greatly improved our ability to link *P–T–d* and age data in low-grade rocks (e.g. Janots et al., 2009); however, successful data acquisition is challenged by small grain sizes and the rarity of the relevant phases. Moreover, preliminary thermodynamic data for REE phases (Kelsey et al., 2008; Spear, 2010; Spear & Pyle, 2010) potentially lead to large *P–T* errors of the stability fields involving these phases, or even more fundamental questions about the relative timing of accessory minerals' appearance (Kohn et al., 2015). Partial resetting during complex fluid–rock interaction (e.g. Grand'homme et al., 2016) may additionally jeopardize the age interpretation. Using a sample from the Staufen-Höllengebirge Nappe (SHN) (Austroalpine Unit, Eastern Alps, Austria) we introduce a novel method that directly relates *P–T–d* estimates derived from thermodynamic modelling of porphyroblast phase relations and chemical compositions with U–Pb geochronological information from micro-zircon inclusions within the same porphyroblasts.

2 | GEOLOGICAL SETTING

The Austroalpine unit in the Eastern Alps is a nappe stack that was built from material of the Adriatic continental crust in the Cretaceous and then became the upper plate during the subsequent closure of the Alpine Tethys and collision of the European plate in the Cenozoic era (Figure 1a; Froitzheim et al., 2008; Schmid et al., 2004). Its tectonostratigraphic age is constrained by the synorogenic sediments on top of the cover nappes (140–100 Ma; Ortner et al., 2008) and by *P–T–t–d* data in the upper greenschist to eclogite facies nappes that together form a metamorphic extrusion wedge (100–85 Ma; Sölva et al., 2005; Tenczer & Stüwe, 2003; Thöni, 2006). The samples investigated in this study were collected at the base of the SHN, the upper structural level of the Austroalpine unit exposed in the Kitzbühel mountains north of the Tauern Window (Figure 1b, Pestal et al., 2005). The nappe consists of (a) Neoproterozoic to Carboniferous metasediments and metavolcanics stacked together during the Variscan orogeny between 350 and 300 Ma (Heinisch et al., 2015), (b) a Permian to Jurassic cover sequence, and (c) Valanginian to Barremian (140–125 Ma) synorogenic sediments (Ortner et al., 2008). Alpine deformation and metamorphism documented by K–Ar and $^{40}Ar/^{39}Ar$ white mica ages commenced between 120 and 113 Ma and lasted until 90–95 Ma (Frank & Schlager, 2006; Kralik, 1983). Metamorphic conditions are constrained by Raman spectroscopy of carbonaceous material (RSCM) yielding maximum temperatures between 200 and 400°C with a normal bottom to top field gradient (Rantitsch & Judik, 2009). Preliminary petrological studies in rather high levels of the SHN yielded *P–T* conditions of 350–400°C at 0.3–0.8 GPa in metabasic rocks (Collins et al., 1980) and 320 ± 30°C at 0.49 ± 0.12 GPa in metasediments (Tropper & Piber, 2012). The absence of direct links between the geochronology and *P–T* conditions hampers the interpretation of these data and their integration in a geodynamic model of the Eastern Alps.

3 | METHODS

Samples A and B were collected at the same outcrop at the base of the SHN at E 47.30301°/N 12.392431° (Figure 1b) and were analysed using the following procedures.

3.1 | Rock and mineral characterization

The petrographic and chemical characterization of the rock samples was carried out at the University of Vienna (Austria). Polished thin sections cut in the XZ plane of finite deformation were investigated using a FEI Inspect S scanning electron microscope (SEM) equipped with a tungsten hairpin electron source operated at 15 kV acceleration voltage. High-resolution images of micro-zircon were captured on a FEI Quanta 3D FEG SEM equipped with a field emission gun which was operated at 10–15 kV acceleration voltage and a probe current of ~4 nA. Zircon was identified by EDS analysis using an EDAX Pegasus Apex 4 system consisting of an Apollo XV Silicon Drift Detector. Large (>3 μm in length) crystals yielded a pure zircon EDS spectrum, however, small crystals yielded an EDS signal which was polluted by the silicate host phase. From similar characteristics compared to larger zircon crystals (Z-contrast, crystal shape), we assume that small, Zr-bearing crystals are zircon as well. The absence of a Ca- or Ti-peak excludes zirconolite ($CaZrTi_2O_7$), and

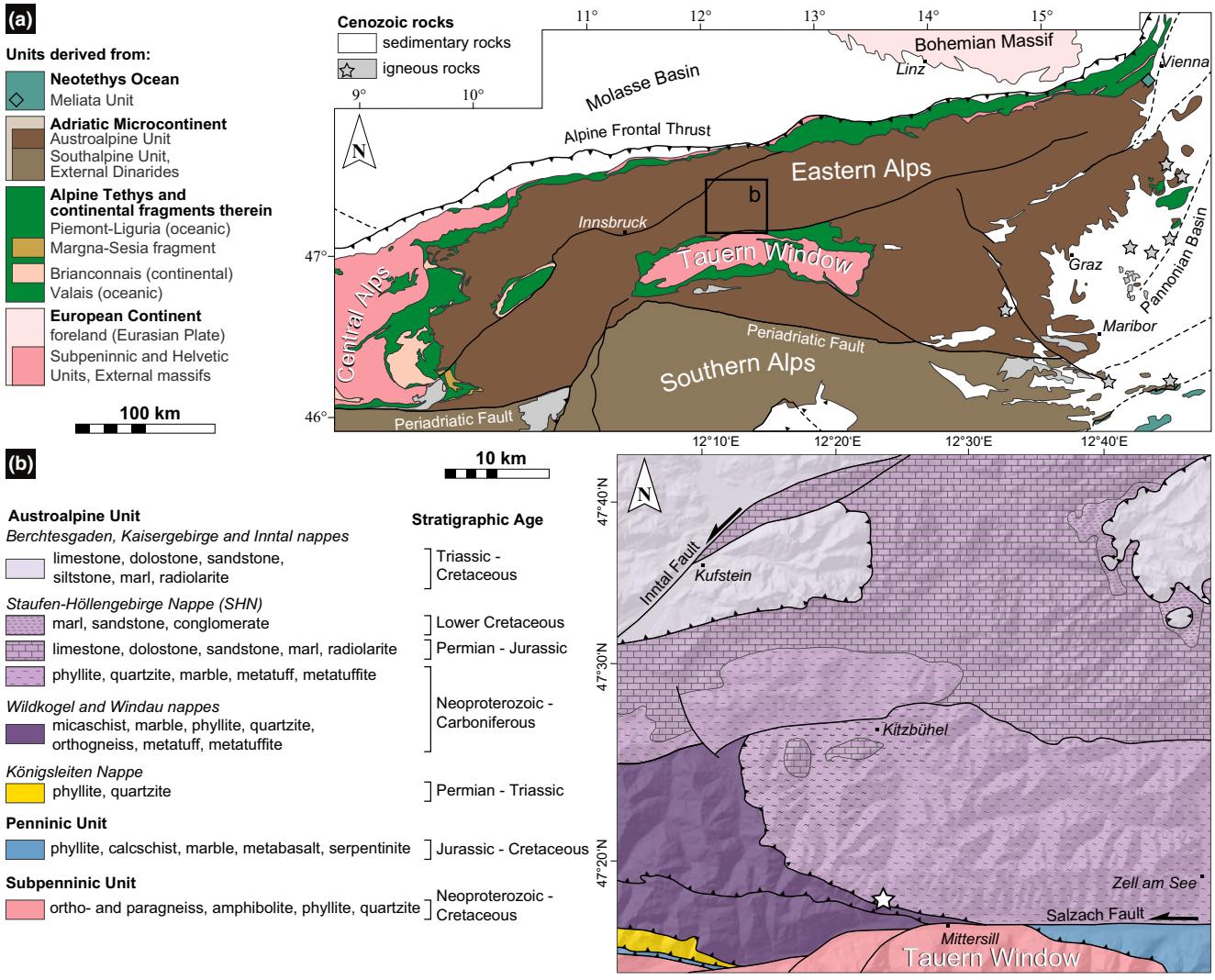

FIGURE 1 (a) Overview map of the Eastern Alps showing palaeogeographic affiliation of the main tectonic units (modified after Froitzheim et al., 2008). (b) Simplified geological map of the Kitzbühel mountains showing the nappes and their lithological contents (modified after Pestal et al., 2005). The star indicates the sample location

baddeleyite (ZrO_2) is highly unlikely given the elevated bulk rock silica content. Therefore, the presence of a detectable Zr peak in the EDS spectrum gives sufficient evidence for zircon (Dempster et al., 2008).

Mineral chemical analyses were carried out with a field emission gun-equipped Cameca SXFiveFE electron probe microanalyser (EPMA), using a 15 kV acceleration voltage, a beam current of 10–20 nA and a spot size of 1 μm (for garnet, chloritoid, ilmenite, rutile) and 5 μm (for muscovite, chlorite). Analytical details are provided in Ntaflos et al. (2017); the full EPMA data set is in Table S1. Apatite analyses were obtained using 20 kV acceleration voltage, 20 nA beam current, and a defocused beam (spot size 8 μm) to minimize damage. Yttrium, La, and Ce were analysed using the Lα-line with TAP (Y) and LLIF (La, Ce) crystals, respectively, and calibrated using synthetic glasses. Structural formulae were calculated following Ketcham (2015). The full data set is provided in Table S2. For whole-rock analyses, the two chloritoid-bearing schist samples selected for thermodynamic modelling were carefully cleaned from macroscopic signs of alteration, crushed and ground to a fine powder. Major and trace elements were analysed by inductively coupled plasma mass spectrometry (ICP-MS) at Activation Laboratories Ltd. (Canada) with additional measurement of FeO by titration and S by infrared analysis. Results are in Table 1.

3.2 | Raman spectroscopy of carbonaceous material

Two graphite-bearing phyllites sampled within 100 m of the chloritoid-bearing schist outcrop were used for RSCM analyses at the University of Leoben (Austria). Carbonaceous matter for the Raman measurements was isolated by an acid treatment. A Horiba LabRAM HR Evolution instrument, equipped with a 100 mW Nd:YAG (532 nm) laser, a

TABLE 1 Whole-rock analyses, model bulk rock compositions and trace element analyses of sample A and B

Whole-rock analysis			Trace element composition			
(w%)	A	B	(ppm)	A	B	avg. upper crust[a]
SiO_2	54.67	48.14	V	215	150	97
TiO_2	2.80	1.29	Ba	515	46	628
Al_2O_3	19.53	17.50	Sr	62	12	320
Fe_2O_3	4.38	5.36	Y	38	52	21
FeO	7.80	16.10	Zr	246	175	193
MnO	0.55	0.83	Cr	170	100	92
MgO	1.98	3.77	Co	24	27	17.3
CaO	0.85	0.58	Ni	70	90	47
Na_2O	0.38	0.03	Cu	60	180	28
K_2O	2.85	0.23	Zn	120	190	67
P_2O_5	0.46	0.40	Rb	68	6	82
Total S	0.03	0.32	Nb	44	23	12
LOI	3.59	4.47	La	41	70.4	31
Total	99.83	98.69	Ce	79.3	134	63
Model bulk composition			Pr	9.22	14.8	7.1
(mol)	**A**	**B**	Nd	37.2	57.1	27
Si	53.79	48.67	Sm	8.1	12	4.7
Ti	2.07	0.97	Eu	2.61	3.31	1
Al	22.64	20.85	Gd	8.4	11.9	4
Fe	9.66	17.38	Tb	1.3	1.8	0.7
Mn	0.45	0.7	Dy	6.9	10.3	3.9
Mg	2.9	5.68	Ho	1.3	1.9	0.83
Ca	0.26	0.05	Er	3.4	5.3	2.3
Na	0.72	0.05	Tm	0.46	0.75	0.3
K	3.57	0.29	Yb	2.8	4.6	2
O	162.01	154.97	Lu	0.4	0.68	0.31
H_2O	25	25	Hf	5.1	3.7	5.3
*X*Mg	0.23	0.25	Ta	3	1.8	0.9
XFe^{3+}	0.20	0.05	Pb	24	< 5	17
			Th	6.5	11.4	10.5
			U	1.1	2.6	2.7
			Th/U	5.9	4.4	3.9

[a]Rudnick et al. (2003).

confocal microscope (hole aperture: 100 μm), a 1,800 g/mm grating, and a Peltier cooled charge-coupled device detector was used to collect Raman spectra. Two scans in the 700–2,000 cm^{-1} region, divided in four 20 s accumulations, were averaged. Several spectra were recorded for each sample and the band positions were maintained by using reference standards. The Raman spectra were evaluated by the Iterative Fitting of Raman Spectra (IFORS) approach of Lünsdorf and Lünsdorf (2016), excluding subjectivity in curve fitting. The results were used to estimate metamorphic temperatures from the regression of the scale total area parameter against metamorphic temperatures of thermometrically well-constrained reference samples (Lünsdorf et al., 2017). To avoid any bias arising from the sample preparation method and instrumental settings, the reference samples were prepared and analysed in an identical manner as the unknowns. Results are presented in Table S3.

3.3 | Thermodynamic modelling

Equilibrium assemblage diagrams were calculated using the Theriak/Domino software package (De Capitani & Petrakakis, 2010). Calculations were performed using the

database file td-tcds62-6axmn-03.txt (http://dtinkham.net/peq.html) compiled by D. Tinkham (Laurentian University, Canada) and combining the tc-ds62 thermodynamic data set (Holland & Powell, 2011) and mineral activity–composition relations in the MnNCKFMASHTO system (White et al., 2014). The white mica model was modified to account for pyrophyllite substitution (Coggon & Holland, 2002). The equilibrium bulk composition for thermodynamic modelling was calculated from whole-rock analyses with modifications of the CaO and FeO to account for phases not considered in the model and ferric iron (X_{Fe}^{3+}) content estimated from *P–X* pseudosections at fixed temperature (see Appendix S1 for details). The unusually high bulk MnO content of the samples required minor modifications of the thermodynamic properties of Mn end-members of chloritoid and ilmenite in order to correctly reproduce observed assemblages and compositions (see Appendix S2 for details). A minimal absolute error of 30–50℃ and 0.1 GPa can be assumed for all *P–T* constraints with the uncertainty on X_{Fe}^{3+} being probably the largest source of error (Plunder et al., 2012; Powell & Holland, 2008).

3.4 | Image analysis

We determined the abundance, size, and distribution of U-bearing accessory phases using image analysis. The drastic difference of phases regarding their abundance and size required the acquisition of two data sets: one high-resolution (pixel width: 0.02 μm) data set for zircon and one lower resolution data set for larger accessory phases of interest (apatite, epidote, rutile). High-resolution images collected during the rock and mineral characterization step were stitched together and loaded into Fiji (imagej.net; Schindelin et al., 2012) where a grey value threshold corresponding to the Z-contrast of zircon was applied. The image was then converted to binary and an erosion algorithm was applied to reduce effects of oblique chloritoid–zircon phase boundaries with respect to the thin section surface, which appear blurry in the image. The binary image was then vectorized in QGIS (qgis.org). Since zircon and rutile have overlapping Z-contrasts, polygons of the resulting data set were manually checked to verify they represent zircon and removed if otherwise. Zircon aggregates were separated in order that each polygon represents a single zircon, or treated as a single zircon where no grain boundary was discernable. The resulting 2,580 zircon polygons were classified according to their microstructural position (e.g. host mineral, location at a grain/phase boundary or included in a host mineral). From the resulting data set, the zircon area and long axis (approximated from diameter of polygon-enclosing circle) were derived (Table S4). For crystal size analysis, an equivalent radius defined by the square root of the area divided by Pi was calculated. Very small, poorly defined crystals (equivalent radius <0.04 μm) were removed from the data set. The zircon orientation was determined from the long axis of best-fit ellipses of zircons (Szpak et al., 2014). For the orientation rose diagrams, isometric crystals with an aspect ratio of ellipse axes between 0.95 and 1.05 were excluded from the data set. Although the digitizing procedure may introduce errors in the area of individual, particularly small grains, general trends concerning crystal size in different domains are valid.

Coarser grained accessory phases (apatite, epidote, rutile) were assessed with respect to their maximum expected contribution to the LA-ICP-MS analysis of the chloritoid rim. We imaged 36 apatite grains, 210 epidote grains, and 298 rutile grains (single crystals or aggregates) in the rims of 10 chloritoid porphyroblasts that were then manually digitized in QGIS to determine their area. Grains that lie within a circle with a diameter of 120 μm (corresponding to the diameter of the laser ablation spot) were grouped into clusters to calculate the areal contribution to the ablated chloritoid. Grain clusters were chosen to maximize the area of the resulting cluster in order to obtain a maximum estimate of the area contribution of these phases.

3.5 | LA-ICP-MS analysis

A Resonetics M-50 193 nm ArF Excimer laser ablation system coupled to an Agilent 7700x quadrupole ICP-MS system (University of New Brunswick, Canada) was utilized for the U–Pb analyses, following the protocol of McFarlane and Luo (2012). Single spot analyses were completed on a polished thin section with the laser operated at a repetition rate of 4 Hz, spot size of 120 μm for chloritoid rim and 20 μm for apatite, pulse energy of 4 J/cm^2, and 30 s of ablation preceded by 30 s of gas background collection. We chose ablation regions in the chloritoid rim which were devoid of inclusions that are detectable with an optical microscope. Isotopes of ^{206}Pb, ^{207}Pb, and ^{238}U were collected with 50, 70, and 20 ms dwell times, respectively, and 10 ms for ^{232}Th and ^{208}Pb. Reference material NIST610 and NIST612 were used as primary standards. Isotope working values for Pb/U in NIST610 are from Horn and von Blanckenburg (2007) whereas those for NIST612 were measured in-house relative to NIST610. Reference standards were analysed under the same conditions as the unknowns. Although no secondary standards for the bulk inclusion method exist, chloritoid from the Jumping Brook Metamorphic Suite, Nova Scotia (McCarron et al., 2021), was analysed using the same routine and yielded an age of 420 ± 48 Ma that overlaps with 395 Ma garnet Lu–Hf dates obtained from the same sequence. All data were reduced offline using a combination of Iolite v3.7 (Paton et al., 2011) and VizualAge v2015.06 (Petrus & Kamber, 2012) running under Wavemetrics IgorPro v6.22.

Iolite's U–Pb geochronology data reduction scheme (Paton et al., 2010) performs a down-hole Pb/U fractionation correction, followed by a drift correction, reference material normalization, and uncertainty propagation. The combination of ablation time, crater diameter, fluence, and repetition rate yielded a shallow exponential down-hole fractionation fit for NIST610 and NIST612 which, when applied to the unknowns, minimized residual Pb/U fractionation as observed in the individual time-series data. Analyses that displayed obvious heterogeneity in the time-resolved U–Pb concentrations were removed during this step. Tera–Wasserburg plots of the U–Pb data were calculated using IsoplotR (Vermeesch, 2018).

Trace element analyses of the chloritoid rim were performed using the same analytical system as for U–Pb analyses at an energy density of 4 J/cm^2 at a repetition rate of 3 Hz and a spot size of 112 μm. We analysed the following isotopes: ^{45}Sc, ^{47}Ti, ^{51}V, ^{85}Rb, ^{88}Sr, ^{89}Y, ^{90}Zr, ^{93}Nb, ^{133}Cs, ^{139}La, ^{140}Ce, ^{141}Pr, ^{146}Nd, ^{147}Sm, ^{153}Eu, ^{157}Gd, ^{159}Tb, ^{163}Dy, ^{165}Ho, ^{166}Er, ^{169}Tm, ^{172}Yb, ^{175}Lu, ^{181}Ta, ^{201}Hg, ^{205}Tl, ^{208}Pb, ^{232}Th, and ^{238}U. Calibration was performed using NIST610 and GSE-1G glass. The full trace element data set is provided in Table S5.

4 | RESULTS

4.1 | Sample petrography, mineral chemistry, and *P–T–d* analysis

Two chloritoid-bearing schists were collected at the same outcrop at the base of the SHN (Figure 1b) for *P–T–t–d* analysis. Sample A contains millimetre-scale chloritoid porphyroblasts in a foliated matrix of chlorite, phengitic white mica, and quartz (Figure 2a). Chloritoid is oriented both parallel and oblique to the main foliation, contains an internal foliation delineated by inclusion trails and has strain shadows filled with chlorite and quartz (Figure 2a,b). These observations indicate intertectonic growth of the porphyroblasts. Chloritoid is chemically zoned with a core to rim decrease in Fe and Mn and increase in Mg (Figure 3a). It also exhibits zoning with respect to inclusion distribution

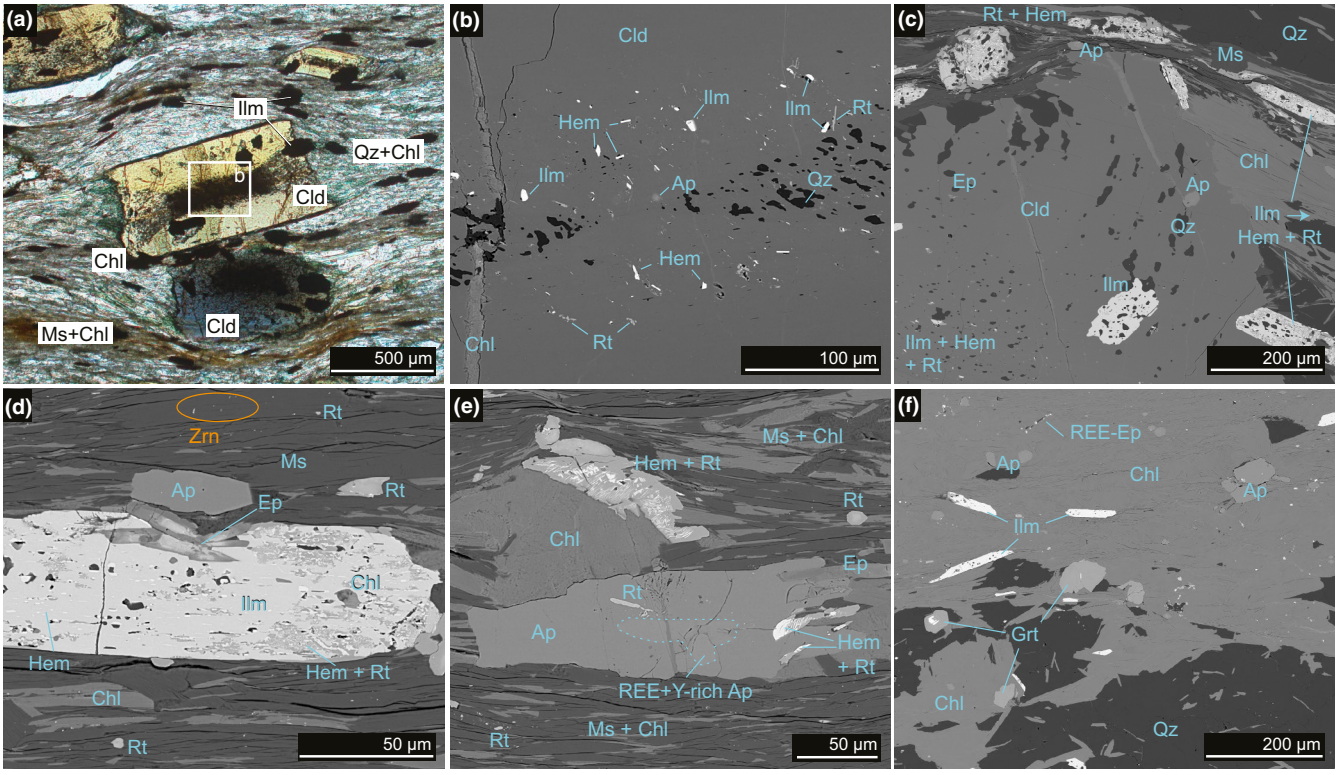

FIGURE 2 Transmitted light microscope (a) and backscattered electron scanning electron microscope (BSE SEM) images (b–f) showing phase relations of sample A (a–e) and B (f). Mineral abbreviations follow Whitney and Evans (2010). (a) Chloritoid porphyroblasts in a matrix of muscovite, chlorite, quartz, ilmenite, rutile, and apatite. (b) Chloritoid core with small inclusions of ilmenite, hematite, rutile, and apatite. The hourglass zoning is defined by quartz inclusions. (c) Different stages of the retrograde reaction ilmenite=hematite+rutile. Ilmenite is best preserved where shielded by chloritoid. Matrix ilmenite is partially to fully replaced. Note the increasing grain size of ilmenite inclusions in chloritoid from core to rim. (d) Matrix ilmenite with chlorite inclusions shows partial replacement by hematite and rutile and overgrows epidote. Note the zoning of epidote with a REE-rich core. (e) Large apatite exhibits chemical zoning with a higher REE+Y concentration in the core. The apatite rim contains rutile inclusions. Note the adjacent ilmenite being fully replaced by hematite+rutile. (f) Small garnet with ilmenite inclusions in a chloritic layer of sample B

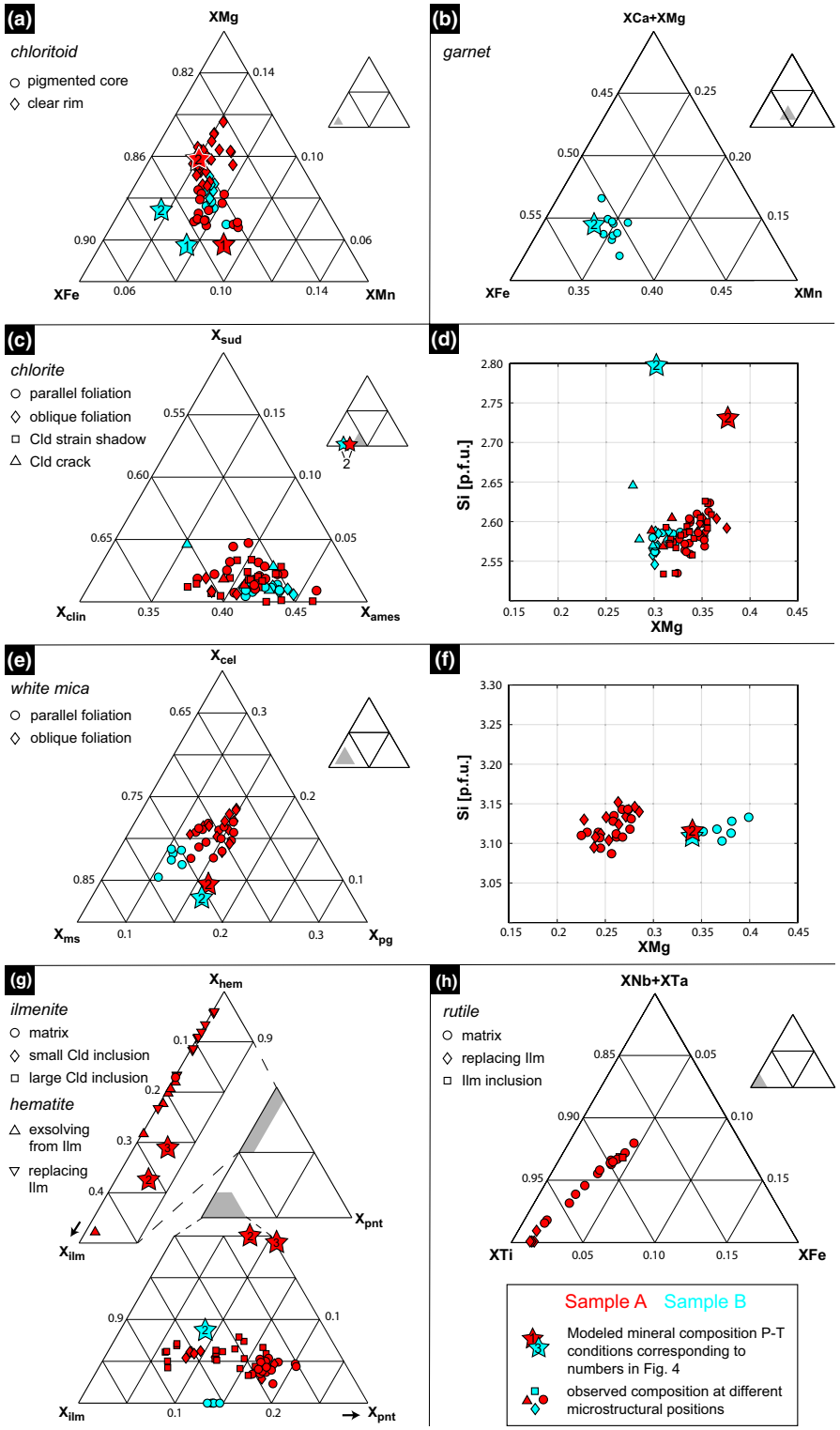

FIGURE 3 Mineral chemistry measured with EPMA for (a) chloritoid, (b) garnet, (c, d) chlorite, (e, f) white mica, (g) ilmenite–hematite solid solutions, and (h) rutile. Modelled compositions are represented as stars. Numbers in stars correspond to prograde stage 1 at 460℃–0.54 GPa, peak stage 2 at 485℃–0.7 GPa and retrograde stage 3 at 450℃–0.5 GPa on Figure 2a. End-member abbreviations according to Whitney and Evans (2010)

defined by a strongly pigmented core with numerous small (<10 μm), euhedral inclusions of zircon, ilmenite, hematite, rutile and subordinate apatite and epidote whereas the rim possesses the same phases but the grain size is markedly larger (Figure 2b,c). Moreover, many chloritoid porphyroblasts exhibit an hourglass zoning defined by quartz inclusions (Figure 2a,b). The oxide assemblage consists of hematite–ilmenite solid solutions and chemically

zoned Nb-bearing rutile (Figure 3g,h). Hemo-ilmenite (X_{hem}~8%) forms up to 200 μm long porphyroblasts containing mostly quartz and occasional chlorite and epidote inclusions (Figure 2d). When hemo-ilmenite is included in chloritoid, its grain size increases from the chloritoid core to the rim (Figure 2c). Unless armoured by chloritoid, it exhibits exsolution patterns with Ti-rich hematite and various stages of replacement by hematite and rutile (Figure 2c–e). Accessory phases are apatite, epidote, and zircon, which are described in detail in Section 4.2. The assemblage chloritoid+chlorite+white mica+ilmenite+hematite+rutile+epidote+quartz is interpreted to represent equilibrium close to peak conditions in sample A. Sample B is a chloritoid–chlorite schist, which in contrast to sample A contains ilmenite as the only oxide phase and a few, small (<100 μm) garnet (Figure 2f). The mineral chemistry of both samples is characterized by high X_{Mn} in chloritoid (0.06–0.09), ilmenite (0.06–0.20), and garnet (0.33–0.36, Figure 3a,b,g; Table S1).

Thermodynamic forward modelling reproduces the peak assemblage of sample A in a narrow stability field defined by the presence of ilmenite, hematite, and rutile and the absence of magnetite, garnet, and margarite at 450–490°C and 0.5–0.7 GPa (Figure 4a). The chloritoid composition of sample A and garnet composition of sample B are modelled along a *P–T* path traversing this field (Figure 4b,c). The prograde and retrograde *P–T* path is constrained by (stage 1–2) the changing chemical composition of chloritoid in the stability field of ilmenite during the prograde path (stage 2) the absence and presence of garnet in sample A and B, respectively, at peak metamorphic conditions at 485°C and 0.7 GPa, and (stage 3) the breakdown of ilmenite to rutile and hematite during the retrograde evolution. The peak temperature of stage 2 agrees with RSCM temperature estimates of 490°C on neighbouring samples (Figure 4a, Table S3). An excellent match of predicted and observed mineral compositions is achieved for chloritoid and garnet, and Si p.f.u. in white mica (Figure 3a,b,f). The observed misfit of modelled and measured mineral composition for chlorite, white mica and ilmenite may be attributed to poorly constrained thermodynamic properties of end-members or solid solution models at low *P–T* conditions and the uncertainty of the bulk rock X_{Fe}^{3+}. Additionally, the chlorite model overestimates Si p.f.u. at low-grade conditions (Figure 3c,d). However, given the excellent fit of thermodynamically well-constrained phases (i.e. garnet) and consistent *P–T* conditions for both samples, we emphasize the robustness of our *P–T* constraints despite slight inconsistencies.

4.2 | Petrography of accessory phases

A detailed description of U-bearing accessory phases (zircon, epidote, apatite, rutile), which are potential targets for U–Pb geochronology in sample A, is provided in the following sections.

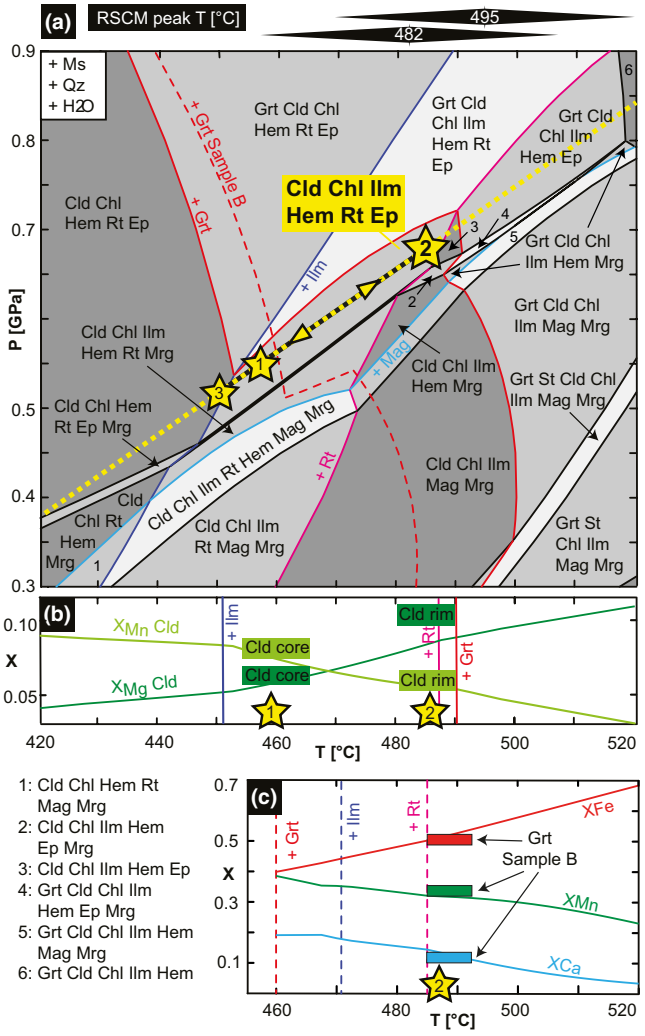

FIGURE 4 (a) *P–T* pseudosection for sample A with results from RSCM thermometry. The garnet-in (Grt) reaction for sample B is indicated. Stars indicate the stages of metamorphic evolution (see text of Section 4.1. for further explanation). Modelled chloritoid composition of sample A (b) and garnet composition of sample B (c) along the prograde *P–T* path (dotted yellow line) show an excellent fit with the measured chloritoid and garnet composition respectively (boxes)

4.2.1 | Zircon

Micro-zircon (mostly <5 μm) is ubiquitous in the matrix and occurs also as an inclusion in all porphyroblasts. No larger zircon exhibiting typical features of a detrital zircon such as a rounded shape and complex internal zoning was observed. We imaged 2,580 zircon crystals in different microstructural domains of sample A, characterizing them in terms of morphology, size, orientation, and spatial distribution.

Zircon inclusions in the chloritoid range between 0.04 and 0.50 μm (equivalent radius) with crystals smaller than 0.25 μm

dominating the spectrum. Zircon generally exhibits straight phase boundaries. Smaller zircons are typically thin, elongate (aspect ratio »1), and lack any internal complexities observable by SEM (Figure 5c–f). By contrast, a few larger zircons have more irregular phase boundaries, have an aspect ratio closer to 1 and may display tiny pores and inclusions (Figure 5g,h). Zircon aggregates consisting of several zircon nuclei are observed at all grain sizes (Figure 5c,d). Rather than being evenly dispersed, zircon is more commonly found forming clusters (Figure 6c,d) and may be aligned along inclusion trails associated with rutile, hematite, and ilmenite in the chloritoid core or alone in the chloritoid rim (Figures 5a,b and 6c). Elongate zircon is preferentially oriented parallel to these inclusion trails (rose diagram, inset in Figure 6c), and no shape preferred orientation parallel to the 001 cleavage of chloritoid is observed.

In core–rim sections of two chloritoid porphyroblasts, 1,297 zircons were imaged and their crystal size distribution (CSD) was statistically evaluated (Figure 6). In both the core and the rim, the minimum zircon size is 0.04 μm and the median zircon size shows only a slight increase from core to rim (0.09 and 0.11 μm respectively). However, the maximum zircon size is significantly larger in the chloritoid rim (0.54 μm) compared to the chloritoid core (0.28 μm). The mean logarithm of the equivalent radius increases from −1.21 ($\sigma = 0.15$) in the chloritoid core to −0.96 ($\sigma = 0.19$) in the chloritoid rim (Figure 6e). We use the zircon area as a proxy to estimate the changes in the zircon volume in different domains. Although there is no significant difference in the total zircon area fraction (0.048% and 0.042% in core and rim respectively), the comparatively large contribution

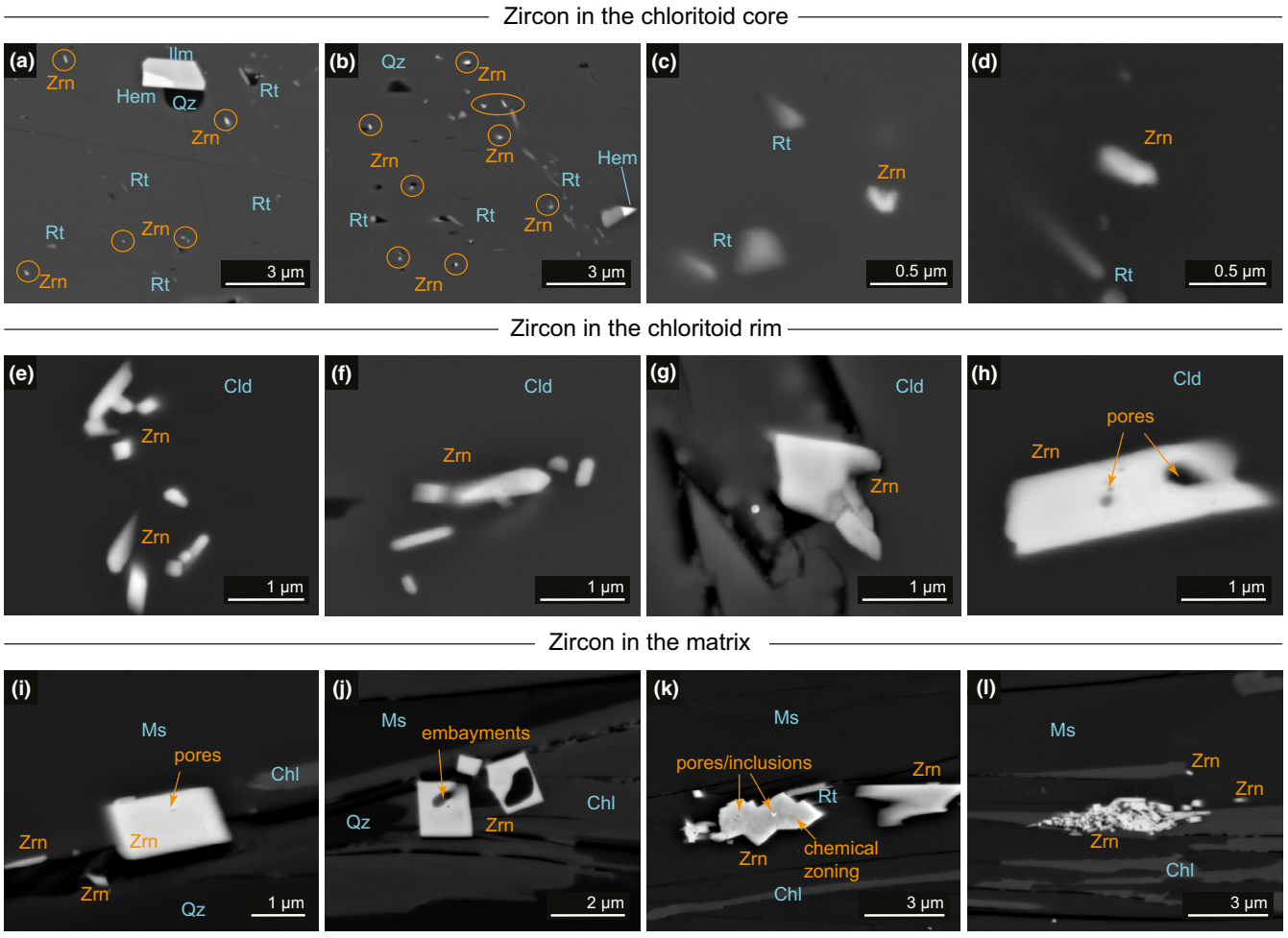

FIGURE 5 BSE SEM microscope images of micro-zircon (Zrn) in chloritoid core (a–d), rim (e–h), and the matrix (i–l). Mineral abbreviations follow Whitney and Evans (2010). Note that phase boundaries that are oblique with respect to the thin section may result in blurred edges. (a, b) Tiny (<0.4 μm) micro-zircon (circled) associated with abundant rutile and occasional hematite and ilmenite along inclusion trails in the chloritoid core. (c, d) Detail of sub-micron scale zircon and rutile. (e–h) Larger micro-zircon in chloritoid rim growing in aggregates or as individual crystals. (g) Note the pores in the largest occurring grains. (i–l) Micro-zircon in the matrix that represents large outliers in the crystal size distribution. These grains may exhibit (i, k) pores and inclusions (j) embayments or (k) variable Z-contrast indicating internal chemical heterogeneity. The bright inclusion in (k) was too small to be identified. (l) Aggregate of submicron-scale zircon that probably formed from recrystallization of a larger zircon grain

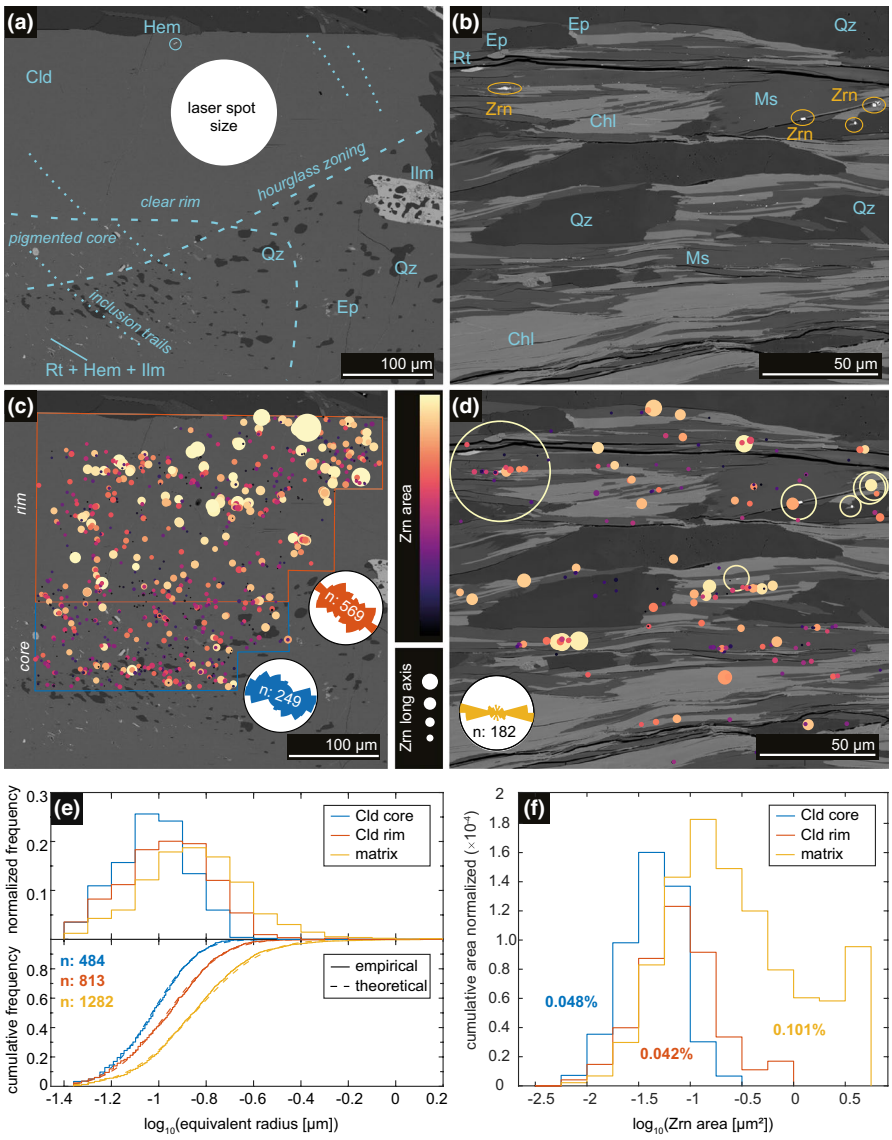

FIGURE 6 BSE SEM images showing the zircon distribution in representative chloritoid core, rim, and matrix regions and results of statistical evaluation of zircon crystal size distribution. Mineral abbreviations follow Whitney and Evans (2010). (a) Overview image showing chloritoid inclusion zonation. Note that the core–rim inclusion zonation is superimposed by an hourglass zonation defined mostly by quartz inclusions. Micro-zircon in the clear rim domain is not discernable due to its small grain size. The size of an ablation region is indicated. (b) Representative overview of a phyllosilicate-rich matrix domain. Note some larger micro-zircons. (c, d) Same overview as in (a) and (b) respectively, with zircon being symbolized as circle coloured according to its area and radius scaled to its long axis. The largest zircons are shown as open circles. Rose diagrams were drawn for zircon with an aspect ratio of >1, showing a shape preferred orientation of elongate zircon parallel to the inclusion trails in the chloritoid and parallel to the schistosity in the matrix. (e) Crystal size distribution of zircon in different domains represented as histograms and cumulative distribution. Note the excellent fit of the empirical cumulative distribution to the theoretical log-normal cumulative distribution function calculated with empirical mean and standard deviation. (f) Zircon areal contribution of each domain. The numbers indicate the integrated fraction of zircon area for each domain. The raw zircon size data are provided in the Supporting information

of the few large zircons in the chloritoid rim is highlighted: the largest 5% comprise 22% of the zircon area (Figure 6f).

Zircon in the matrix ranges between 0.04 and 1.31 µm (equivalent radius), with a median of 0.14 µm and the majority (97%) of zircon is <0.4 µm. These small zircons have the same properties as similarly sized zircon inclusions in the chloritoid. By contrast, the few large outliers exhibit more complex internal features, such as small pores and inclusions, and diffuse variations of the BSE Z-contrast, which is indicative of chemical zoning (Figure 5k). Phase boundaries are mostly straight, although some of the largest zircons exhibit shapes that are more irregular, contain embayments or possess larger pores (Figure 5j). Zircons are isolated or occur as clusters of several grains, and can form aggregates of several nuclei (Figure 5k). In rare cases, these aggregates are composed of more than 20 smaller

zircons (Figure 5l). Zircon show a shape preferred orientation parallel to the main schistosity, which is defined by the basal cleavage of phyllosilicates (rose diagram, inset in Figure 6d).

Statistical evaluation of 1,282 zircons in five arbitrarily chosen locations of the matrix revealed that the majority of zircons (62%) are located at grain and phase boundaries, which accounts for 78% of the total zircon area in the matrix. Zircon is found more commonly in phyllosilicate-rich domains (Figure 6b,d) where it comprises 0.114% of the total area, in contrast to quartz-rich domains (0.022% of the total area). The mean logarithm of the equivalent radius is −0.85 ($\sigma = 0.22$), which is larger compared to those occurring as chloritoid inclusions (Figure 6e). Similarly, the total zircon area fraction is 0.101%, which is significantly larger than in the chloritoid (Figure 6f). This may, however, arise from the fact that more phyllosilicate-rich domains were imaged rather than corresponding to an actual increase in zircon area fraction in the matrix. Similar to the chloritoid rim population, the largest 5% of the matrix zircon population have a large contribution (38%) to the total zircon area (Figure 6f). One-sample Kolmogorov–Smirnov (Davis, 2003) testing indicates that the three zircon populations are from log-normal distributions with means and standard deviations identical to the empirical values (significance level of 5%) corroborated by the excellent fit between the empirical and theoretical cumulative frequency curves (Figure 6e). Two-sample Kolmogorov–Smirnov testing indicates that the sampled populations are from different continuous distributions (significance level of 5%).

4.2.2 | Apatite, epidote, rutile

Apatite is common in the matrix and occasionally enclosed in chloritoid. It forms euhedral, up to 300 μm long grains that are aligned parallel to the main schistosity. Especially larger grains occasionally show chemical zoning with elevated Y and Ce contents in the core (Figure 2e, averaged compositions are in Table 2; the full data set is in Table S2). Both cores and rims indicate that fluoroapatite is the dominant end-member. The REE+Y-free apatite rims contain rutile, hematite, epidote, and zircon inclusions (Figure 2e). The boundary between these zones is straight (Figure 2e) or highly irregular (Figure 7a). Epidote is usually found forming rhomboid-shaped aggregates of numerous, small (<20 μm) crystals or larger (up to 80 μm long) individual crystals, which are euhedral, elongate, and commonly oriented parallel the main schistosity. Most crystals show a distinctive chemical zoning with REE-rich cores and REE-poor rims (Figure 2d) although the cores are not always present (Figure 7c). In chloritoid, it occurs both as small (<10 μm), single crystal inclusions in the core and achieves larger grain sizes (mostly in aggregates) in the rim. Rutile occurs abundantly in the chloritoid core and in the matrix. Two dominant morphological types are distinguished: tiny (<1 μm), needle-shaped rutile is mostly found in chloritoid core where it forms inclusion trails (Figure 5a,b), and larger (1–5 μm), isometric to elongate rutile crystals are occasionally enclosed in the chloritoid rim (Figure 7c,e). In a few cases, distinct zones with a high Nb content are observed (Figure 7e). In the matrix, rutile commonly occurs as ~20–30 μm large euhedral or subhedral crystals (Figure 2d,e) and exhibits core to rim zoning with up to 9 wt% NbO_2 in the core (Figure 3h). Moreover, rutile with low Nb concentrations is found together with hematite growing at the expense of ilmenite (Figures 2c–e and 3h).

TABLE 2 Average apatite core and rim composition sample A[a]

	n = 4		*n* = 7	
(wt%)	avg. core	std. core	avg. rim	std. rim
P_2O_5	41.43	0.28	42.20	0.27
SiO_2	0.42	0.26	0.06	0.09
FeO	0.61	0.23	0.25	0.07
MnO	0.11	0.03	0.07	0.02
MgO	0.07	0.03	0.01	0.02
CaO	53.63	0.52	55.33	0.36
SrO	0.05	0.03	0.03	0.02
La_2O_3	0.13	0.09	0.02	0.04
Ce_2O_3	**0.35**	0.18	**0.04**	0.07
Y_2O_3	**0.30**	0.19	**0.01**	0.03
F	3.91	0.72	3.83	0.33
Cl	0.01	0.00	0.00	0.00
Total	101.04	1.02	101.87	0.58
	a. p. f. u.			
P	5.956	0.049	5.992	0.024
Si	0.072	0.044	0.010	0.015
Fe	0.086	0.033	0.035	0.010
Mn	0.015	0.005	0.011	0.003
Mg	0.017	0.009	0.002	0.005
Ca	9.757	0.074	9.942	0.041
Sr	0.005	0.003	0.003	0.002
La	0.008	0.005	0.001	0.002
Ce	**0.022**	0.011	**0.002**	0.004
Y	**0.027**	0.017	**0.001**	0.003
F	2.100	0.381	2.032	0.170
Cl	0.000	0.000	0.000	0.000
Σ P site	6.028	0.092	6.002	0.038
Σ Ca site	9.938	0.157	9.998	0.071

Note: Bold values highlight the differences in the Ce and Y content of the core and rim domains.

[a]Structural formulae calculation after Ketcham (2015).

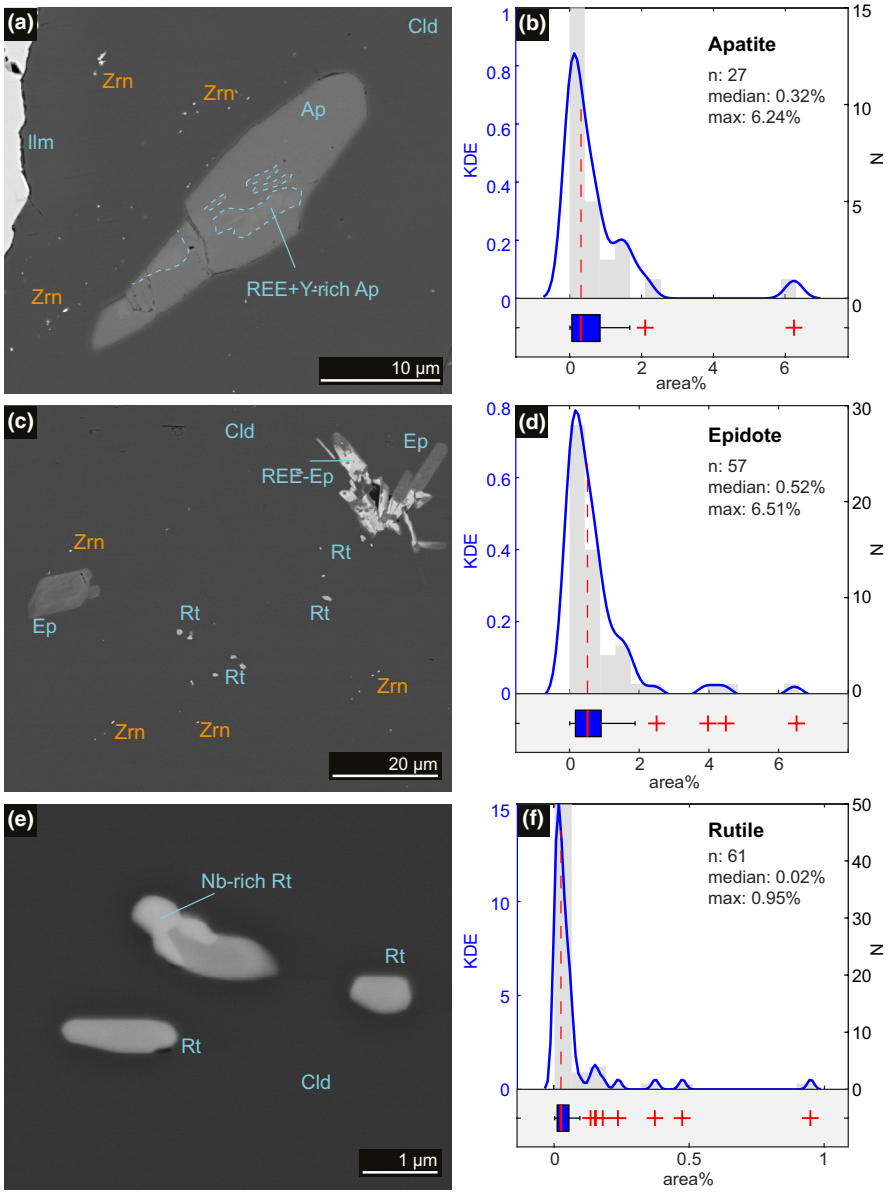

FIGURE 7 BSE SEM images of potential U-bearing accessory phases in chloritoid rim showing (a) a relatively large apatite inclusion with a REE+Y-rich core zone associated with micro-zircon, (c) epidote and rutile clusters enclosed in chloritoid rim, (e) small rutile inclusions with a distinct Nb-rich zone. The histogram, KDE function, and boxplot of area contribution of clusters of each phase to an ablation region with 120 µm diameter are shown for (b) apatite, (d) epidote, and (f) rutile. Mineral abbreviations follow Whitney and Evans (2010)

Similar to zircon, epidote, apatite, and rutile grain sizes systematically increase when comparing their presence in the chloritoid core, rim, and the matrix. To estimate their expected contribution to the LA-ICP-MS analysis of the chloritoid rim, the areal proportion of crystals or crystal clusters that lie within a 120 µm circle (corresponding to the laser spot diameter) was determined (Figure 7). Note that the cluster yielding the maximum area was chosen, thus maximizing the contribution of these minerals. Apatite and epidote show a similar cluster size distribution (median: 0.32% and 0.55%; maximum: 6.24% and 6.51% respectively); epidote clusters occur twice as often (Figure 7b,d). Most rutile clusters range between 0% and 0.1% (median 0.02%) with a maximum area proportion of 0.95% (Figure 7f). This is consistent with the observations that rutile is less abundant than zircon, but reaches larger a crystal size (Figure 7c).

4.3 | Laser ablation ICP-MS

4.3.1 | U–Pb isotopic data of epidote, apatite, and chloritoid rim

In sample A, we attempted to date the main metamorphic event by obtaining LA-ICP-MS U–Pb data from accessory minerals that grew during metamorphism. REE-rich epidote, a promising candidate for such an attempt (e.g. Janots et al., 2009), did not yield sufficiently high U and Pb concentrations to calculate a geologically meaningful age. Moreover, the mineral's small size mostly prevented analysis of single growth zones of individual crystals. LA-ICP-MS U–Pb analyses of apatite in sample A yielded a lower intercept age in Tera–Wasserburg space of 429.3 ± 14.7 Ma (*n*: 59, MSDW: 1.2; Figure 8a, Table S6). Apatite analyses generally exhibit high common Pb concentrations with

the majority of the data plotting close to the y-intercept at $^{207}Pb/^{206}Pb_0 = 0.851 \pm 0.003$. The positive correlation of U and Y (Figure 8a) suggests that analyses with higher U/Pb ratios likely stem from apatite cores.

Although it is challenging with any presently available analytical technique to extract quantitative isotopic or geochemical analysis of the individual micro-zircons, we attempt to derive such information from the bulk zircon population included in the chloritoid rim using LA-ICP-MS analysis. To maximize the zircon signal, a laser spot diameter of 120 µm was employed for ablation and larger inclusions detectable with reflected light microscope were avoided. From the U–Pb isotopic data, a Tera–Wasserburg lower intercept age of 116.7 ± 9.1 Ma (*n*: 79, MSDW: 1.5) was calculated (Figure 8b, Table S7). Most analyses lie close to the y-intercept, indicating that common Pb dominates the isotopic signal. The intercept at $^{207}Pb/^{206}Pb_0$ 0.840 ± 0.005 is consistent with terrestrial $^{207}Pb/^{206}Pb_0$ of 0.843 at 120 Ma as predicted by the model of Stacey and Kramers (1975).

4.3.2 | Trace element data of bulk inclusions in chloritoid rim

We performed additional LA-ICP-MS trace element analyses of chloritoid rims to characterize the source of U, Th, and Pb (Figure 9, Table S5). Most analyses yield relatively low U, Th, REE, and Y concentrations except for three outliers (shown as red squares in Figure 9a–d; scaling factor indicated in the upper right corner of the diagrams). Zirconium (up to 350 ppm) is positively correlated with U, with only five analyses yielding Zr of <10 ppm and where U is below the detection limit. Most analyses follow a linear trend (Zr/U ~ 320). Few analyses that deviate from the trend have an elevated Y content. Yttrium and uranium are positively correlated as well, and several linear trends can be distinguished (Figure 9b). Analyses characterized by a very low Sr content of <0.5 ppm dominantly plot along a well-defined Y/U of 8. Analyses with Sr ranging between 0.5 and 2 ppm scatter around a trend that follows Y/U of 13. Four analyses with elevated Sr and Y define a separate linear trend above the main group—these are the same analyses, which deviate from the main Zr–U trend. Three outliers (red squares in Figure 9b, scaled by factor 15) follow a different, much steeper trend. No correlation between Sr (up to 13 ppm, outliers excluded) and U was found; however, elevated Sr correlates with higher Ce (up to 11 ppm, Figure 9c). Significant amounts of Ti (up to 31,100 ppm), which is positively correlated with Nb (up to 116 ppm) were detected, yet no systematic correlation between Ti and U concentrations was observed (Figure 9d). The majority of analyses follow a linear trend with a Ti/Nb ratio of 400; few points plot on a steeper trend (Ti/Nb ~33).

The trace element data set is compared with the U–Pb data set of chloritoid rim and U–Pb data set from matrix apatite in terms of U–Th systematics. Apatite core analyses have the highest U concentrations (up to ~8 ppm) and scatter around the trend defined by Th/U of ~4. Three outliers from the trace element data set show much higher Th/U ratios of ~25 (Figure 9e). The majority of all data are characterized by low U (<1.5 ppm) and Th (<4 ppm) concentrations (Figure 9f; note that analyses represented by squares are scaled by a multiplication factor of 10). Apatite core analyses tend to have higher Th/U ratios, in contrast apatite rim analyses show a larger variation (Th/U = 1–10). The lower limit of Th/U = 1 is well-defined by all three data sets. The trace element data mostly plot along the Th/U of ~1 and few have higher Th/U values of ~4; no systematic correlation between an elevated Th/U ratio of ~4 and a different element (e.g. Ce, Y, Sr, Ti) is obvious. The chloritoid rim U–Pb data set shows similar characteristics, although few analyses have even higher Th/U values of 4–12.

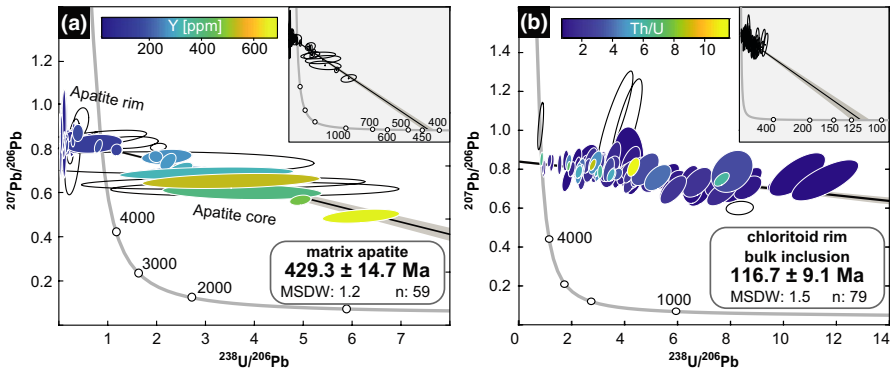

FIGURE 8 Tera–Wasserburg diagrams of (a) LA-ICP-MS U–Pb matrix apatite and (b) chloritoid rim bulk inclusion analyses of sample A. Insets show the full Tera–Wasserburg diagram including the lower intercept with the Concordia curve, which defines the age. The colour indicates (a) the Y concentration in apatite and (b) the Th/U ratio of bulk inclusions. Analyses represented as open ellipses were discarded for age calculation. Age ticks on the Concordia curve are given in (Ma). Data are shown at 2σ errors. See Supporting information for data tables

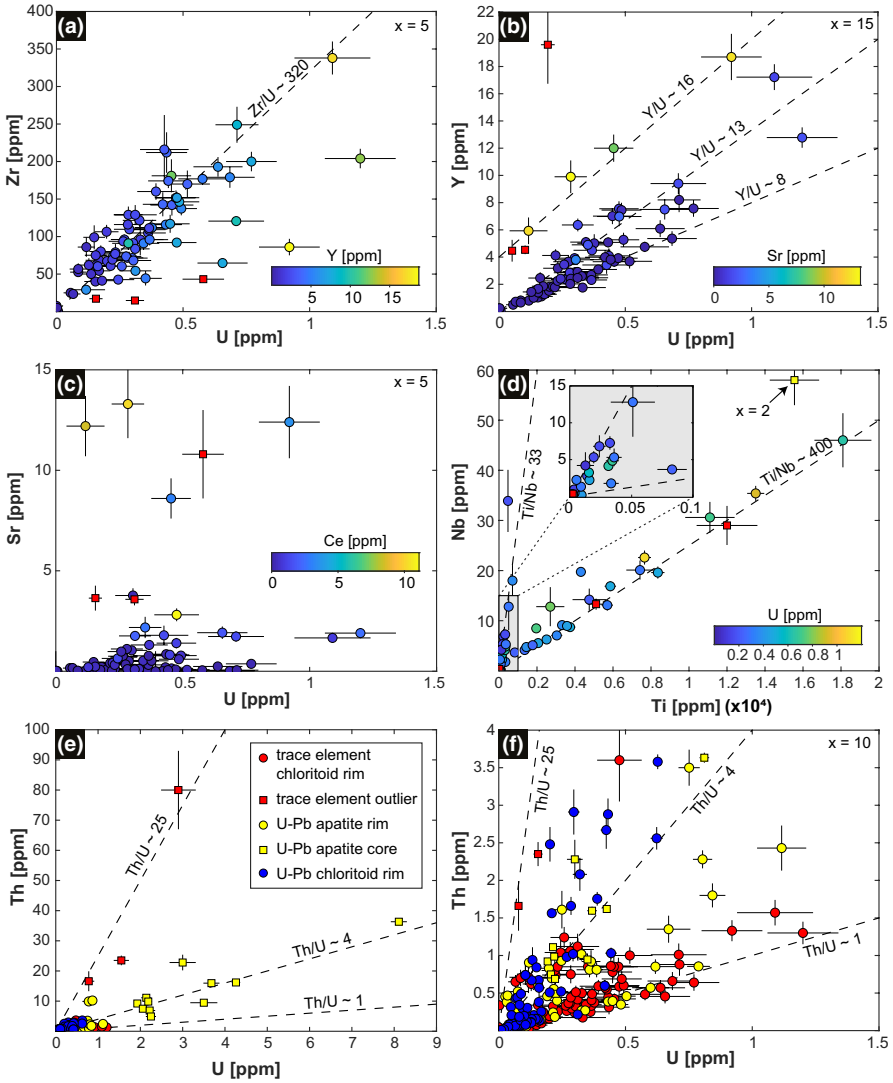

FIGURE 9 Chloritoid rim bulk inclusion LA-ICP-MS trace element analyses showing the relationship between (a) U and Zr, (b) U and Y, (c) U and Sr (d) Ti and Nb, and (e, f) U and Th. Marker colour represents the concentration of (a) Y, (b) Sr, (c) Ce, and (d) U respectively. Red squares in (a–d) are outliers and shown scaled by a multiplication factor given in the upper right corner of each plot. (e) Comparison of the U–Th systematics of the trace element data set and the U–Pb data sets of apatite and chloritoid rim. (f) Zoomed view of (e), analyses represented as squares are scaled by a factor of 10. See Table S5 for the full trace element data set

5 | DISCUSSION AND CONCLUSION

We have successfully acquired *P–T–t–d* data on low-grade metamorphic samples of the SHN by conducting an innovative approach on chloritoid porphyroblasts that resulted in a U–Pb date (116.7 ± 9.1 Ma) and conditions of metamorphism (450–490℃ and 0.5–0.7 GPa). Our geochronologic data are relatively precise, with modest errors and small MSWD values, and are geologically realistic. However, we must evaluate which phase(s) were analysed to make an informed interpretation.

5.1 | Formation of the accessory minerals

From petrographic relationships and geochronological data, we can establish the timing of growth of the U-bearing phases. In metapelites, zircon is typically a detrital phase, although small-scale Zr mobility and the growth of metamorphic zircon have been documented at low-grade metamorphic conditions where it can form outgrowths on detrital zircon grains (Dempster et al., 2004; Kelly et al., 2017; Rasmussen, 2005). Our sample A, however, lacks zircon exhibiting typical features of a detrital phase that record a complex history. By contrast, the zircon is mostly small, unzoned, and euhedral indicating a single-phased growth event. The lack of detrital zircon can be explained in two ways: Either it was absent from the protolith, which is unlikely given the relative high bulk Zr content (246 ppm, Table 1; Rudnick et al., 2003), or all the detrital zircon grains were consumed by the growth of a metamorphic Zr-bearing phase. In the matrix of our sample A, zircon is particularly abundant at grain and phase boundaries, especially in phyllosilicate domains, and the chains of many small zircons oriented parallel to the schistosity likely indicate syntectonic formation (Didier et al., 2014). The prevalence of zircon along the metamorphic planar fabric of the rock and its shape preferred orientation parallel to this fabric support the conclusion that zircon is metamorphic (Dempster et al., 2008). Zircon inclusions in chloritoid

exhibit no preferred orientation relative to its crystallographic planes, thus precluding exsolution of zircon after crystallization of chloritoid as a growth mechanism.

The analysis of CSD may provide additional insight. Note that in the present case, the two-dimensional data can be extrapolated to three dimensions (Higgins, 2000) since zircon crystals were studied in a thin section cut perpendicular to the schistosity and parallel to the lineation, and prismatic zircon crystals can be approximated by a parallelepiped. The observed zircon populations have a very well-defined distinct log-normal CSD in the three microstructural positions (chloritoid core, chloritoid rim, and matrix). Grain size reduction due to cataclastic deformation or dynamic recrystallization of zircon could produce such a log-normal CSD (e.g. Phillips & Williams, 2021; Shimizu, 1999), however, given the lack of evidence supporting these processes, it is more likely that the observed CSD is due to the zircon nucleation and growth processes. Theoretical derivations and experiments demonstrate a log-normal CSD can either result from nucleation followed by surface-controlled growth (Kile et al., 2000 and references therein) or from random nucleation and growth with a decreasing nucleation rate controlled by limited reactant supply (Bergmann & Bill, 2008). Both models align with the notion that the zircon is metamorphic and nucleated at some point during metamorphism. The second model may be valid for our sample A since limited reactant supply appears to be realistic given the finite amount of Zr in the rock.

We conclude that the three measured CSDs demonstrating progressive coarsening from chloritoid core to the matrix reflect a single zircon population characterized by a single set of nucleation and growth parameters. The three distributions represent a logical evolution of the same crystal population with time. In this framework, the oldest preserved stage is frozen in chloritoid cores, an intermediate stage is found in the chloritoid rim and the matrix contains the final stage. The results of our study document extensive nucleation of micro-zircon during prograde low-grade metamorphism, similar to Dempster et al. (2008) who reported sequential crystallization and dissolution of micro-zircon during amphibolite facies metamorphism. Contrary to these authors who postulate precipitation of micro-zircon during the prograde evolution followed by dissolution at peak metamorphism, we interpret that zircon precipitation commenced on the prograde metamorphic path prior to chloritoid growth and continued at least until peak metamorphism was achieved. Only the largest zircons in the matrix exhibit features that can be interpreted as signs of dissolution (porosity, embayments), which likely occurred during retrogression. The lack of dissolution may be explained by the fact that zircon grew prior to crystallization of garnet, which can incorporate significant amounts of Zr (e.g. Degeling et al., 2001) and probably promotes micro-zircon dissolution.

We can only speculate on the exact mechanisms of zircon growth and transport of Zr as well as the Zr source. The shape, the preferred orientation, and the preferred occurrence of zircon at grain and phase boundaries in the matrix suggest that these grains precipitated from a Zr-saturated fluid that migrated along boundaries (Dempster et al., 2008; Hay & Dempster, 2009). Zircon occurring more abundantly in phyllosilicate-rich layers may be an effect that these domains have a higher density of boundaries, hence more theoretical nucleation sites would have existed. It could also demonstrate a structural or mineralogical control (or combination) of zircon nucleation sites (Dempster et al., 2008; Hay & Dempster, 2009). Rasmussen (2005) suggested that Zr can be transported in a fluid within a halogen complex and that fluorine plays a crucial role in the Zr solubility. This may be applicable to our sample as the crystallization of metamorphic fluoroapatite rims suggests that fluorine was present in the metamorphic fluid. Although there is no clear evidence for a potential source of initial Zr, we can consider likely candidates. The most likely candidate is detrital metamict zircon that is readily dissolved under greenschist facies conditions (e.g. Dempster et al., 2008; Rasmussen, 2005). It is, however, unusual that no detrital remnants survived low-grade metamorphism. Other possibilities include detrital phases that contain more modest amount of Zr and U and that became unstable during metamorphism, such as igneous titanite (Cherniak, 2006; Ventura et al., 1999) or ilmenite (Bingen et al., 2001). Detrital titanite and ilmenite would also account for a Ti source of the metamorphic Ti-bearing phases. If the source material of the sedimentary protolith involves mafic volcanic material, detrital baddeleyite is also an option (Heaman & LeCheminant, 1993).

The timing of apatite, epidote, and rutile growth is in comparison easier to pin down. New apatite LA-ICP-MS dating yielded a pre-Variscan date of 429.3 ± 14.7 Ma. Microstructural evidence such as the overgrowth over metamorphic phases (e.g. rutile, hematite, and epidote) suggests crystallization of apatite during metamorphism. Combining the apatite chemistry and U–Pb data, it is apparent that metamorphic apatite is depleted in REE, Y, and U, consistent with that of Ribeiro et al. (2020), and it is most likely that the apatite date can be linked to the inherited REE+Y-rich cores. The preservation of inherited apatite dates is not unexpected since the metamorphic temperatures of the sample (490°C) did not exceed the range of closure temperatures for Pb diffusion in apatite (350–550°C; Engi, 2017 and references therein). Removing some of the low-U rim analyses, which lie slightly below the isochron, shifts the lower intercept towards older apparent ages (474.3 ± 16.5 Ma, *n*: 27, MSWD: 0.7), thus the *c*. 429 Ma is interpreted as the minimum age of protolith formation. The temporal constraint for this rock in the middle Silurian is consistent with the Neoproterozoic to Carboniferous deposition age for the metasediments and

metavolcanics within the SHN (Heinisch et al., 2015; Pestal et al., 2005). The abundant Ordovician volcanism (Loeschke & Heinisch, 1993) is also in line with a dominant pre-Silurian source. We interpret that epidote and rutile grew during metamorphism, which is supported by thermodynamic modelling. Furthermore, similar to zircon, petrographic observations (i.e. euhedral shape, increasing grain size comparing chloritoid inclusions and matrix grains) suggest progressive coarsening over time.

5.2 | Interpretation of the chloritoid rim LA-ICP-MS data

Very low U and Zr concentrations in some trace element analyses of the chloritoid rim suggests that these elements do not substitute in the chloritoid crystal lattice and can thus be predominantly attributed to inclusions. This is unsurprising considering that no position in the chloritoid crystal lattice is favourable for U substitution, and hence, the term 'bulk inclusion' seems appropriate. Using results from trace element analysis combined with petrographic evidence we can qualitatively estimate the proportions and compositions of inclusions and their influence on the U–Pb isotopic data.

Petrographic observations revealed that micro-zircon is by far the most abundant inclusion phase in the chloritoid rims. The correlations that we identified between U, Zr, Y, and HREE, which are typically present in zircon in abundance (e.g. Rubatto, 2002), suggest that the micro-zircon inclusions are likely the major source of U and Pb in our analyses. Assuming a simple substitution of U for Zr, the expected amount of U in zircon can be calculated. The observed Zr/U ratio of 320 corresponds to a U concentration of ~1,550 ppm in zircon, which is consistent with published zircon data (Rubatto, 2017 and references therein). Calculating the amount of Zr in a chloritoid volume that contains 0.042 vol.% zircon (approximated from the mean area contribution, Figure 6f) yields 280 ppm, thus petrographic constraints on the amount of zircon are consistent with results from trace element analysis.

Other inclusions in the chloritoid rim that may have potentially contributed to the bulk inclusion U–Pb signal include rutile, epidote, and apatite. These inclusions are much less abundant compared to zircon; however, given their larger size, they may have a relatively larger contribution to the ablation volume. Of the trace element analyses, 77% of the data yield a Ti content of >10 ppm, which correlates with elevated Nb, suggesting some amount of rutile in the majority of the analyses. The perception of two distinct chemical trends agrees with the observation of few high Nb rutile grains and a majority of low Nb rutile. Since neither Ti nor Nb are correlated with U content, it can be assumed that rutile does not affect the bulk inclusion U–Pb data. Three analyses display REE, Y, Sr, U, and Th contents that are orders of magnitudes higher than the rest of the data set. Considering the high Th/U ratio, it is most likely that this can be attributed to larger inclusions of REE-rich epidote (Gieré & Sorensen, 2004).

Rare elevated Sr concentrations that correlate with high Y concentration, which were observed in the trace element data set, may indicate apatite inclusions. A large proportion of apatite in the analytical volume would be indeed problematic, as the evidentially older apatite core domains could result in a bias towards older ages. To estimate whether this has a significant effect on the U–Pb age, the contribution of apatite to the total U budget in the chloritoid rim was calculated, assuming a simplified model considering only zircon and apatite. The fraction of U coming from apatite can be expressed as a function of the ^{238}U concentration in apatite ($^{238}U_{Ap}$) and zircon ($^{238}U_{Zrn}$) and the mass fraction of apatite, which is determined from the area fraction of apatite and zircon calculated from image analysis. The $^{238}U_{Ap}$ concentration is known from the apatite U–Pb data and the $^{238}U_{Zrn}$ concentration can be derived from the Zr/U ratio of the trace element data set (see Appendix S3 for the derivation). Using median values for all variables, U from apatite contributes 0.12% to the total measured U value. Assuming the maximum apatite fraction or the maximum U concentration in apatite yields an apatite contribution of 2%–3% when all other values are kept at median. Note that all these values are overestimated since they assume the presence of an apatite cluster in the ablated region (see Section 3.4). However, larger inclusions were avoided by carefully selecting the position of the region of ablation and petrographic observations suggest that inherited cores are only present in some grains, thus the majority of apatite grains included in chloritoid are metamorphic. We emphasize that due to the different size and abundance of apatite (few, large grains) and zircon (numerous, tiny grains), a potential influence of apatite would affect at most just a few analyses, but would not result in a systematic 'drag' of the bulk inclusion U–Pb trend towards older apparent ages. In the unlikely event that a large, U-rich apatite was present in the ablated chloritoid volume, the corresponding ellipse would lie below the main trend on the Tera–Wasserburg plot and can therefore be excluded from the age calculation.

The majority of trace element analyses have a Th/U value of ~1, which is principally compatible with reported Th/U values for metamorphic zircon (e.g. Garver & Kamp, 2002; Martin et al., 2008; Rubatto, 2002, 2017; Yakymchuk et al., 2018), suggesting that this corresponds to the Th/U ratio of zircon in our sample. Generally elevated Th/U ratios of U-bearing phases are unsurprising considering the relatively high bulk rock Th/U value (Table 1). However, some chloritoid rim U–Pb analyses have higher Th/U values that demand explanation. Small epidote inclusions may be one reason; also, metamorphic apatite with Th/U up to 20 may play a role. The contribution of another, unidentified Th-rich phase (e.g. thorite) cannot be excluded. To determine if the bulk inclusion date is compromised by high Th/U analyses,

we calculated apparent ages on subsets of the bulk inclusion U–Pb data based on the Th/U values. The resulting dates deviate, at most, by 6 m.y. from the age calculated for the full data set (Table 3), thus a perturbation of Th-rich phases is considered as insignificant.

Finally, we have to address the problem that the chloritoid rim bulk inclusion U–Pb data are highly discordant, suggesting a major contribution of non-radiogenic Pb. This is inconsistent with the notion that zircon typically does not incorporate common Pb and yields concordant dates. The vast majority of the zircon literature reports geochemical data of metamorphic zircon that formed at high-grade metamorphic conditions (e.g. Harley et al., 2007; Rubatto, 2017), consequently limiting our knowledge about the chemistry of zircon that formed at low-grade conditions. Experiments investigating the incorporation of Pb in zircon demonstrated that zircon growing at wet-metamorphic conditions in a Pb-rich environment can accommodate common Pb concentrations orders of magnitudes higher than those assumed for high-grade zircon (Watson et al., 1997). These results are applicable to our sample A, given its metamorphic grade and its elevated bulk rock Pb content (Table 1). Aside from zircon, the contribution of other metamorphic phases that can incorporate significant amounts of common Pb may play a role (e.g. apatite: Chew et al., 2011; epidote/allanite: Darling et al., 2012; rutile: Cherniak, 2000). Substitution of divalent Pb in the chloritoid crystal lattice seems unlikely, given its large ionic radius. Regardless of the common Pb host, we stress that the isotopic composition we measured is consistent with the terrestrial Pb composition at 120 Ma (Stacey & Kramers, 1975), suggesting isotopic equilibrium between the different phases at the time of closure of the U–Pb system (i.e. the mineral growth). We conclude that although other inclusions may have been present, the chloritoid rim U–Pb date is dominantly attributed to metamorphic micro-zircon inclusions.

5.3 | Link of *P–T* and *t* and regional geological implications

Calculations using the Pb diffusion coefficient of Cherniak and Watson (2001) resulted in negligible diffusional Pb loss during peak metamorphism even for the smallest (0.04 μm) zircons. Furthermore, we assume that U and Pb loss due to metamictization since the Early Cretaceous is insignificant because the calculated α-decay dose for a 120 Ma zircon containing 1,550 ppm U and Th corresponding to a Th/U ratio of 1–4 is too low to cause significant radiation damage (Ewing et al., 2003; Murakami et al., 1991). Hence, the chloritoid rim U–Pb date can be interpreted as the age of zircon growth. Our zircon CSD data imply continuous zircon precipitation throughout prograde metamorphism, and each laser spot contains variable numbers of zircons that grew over short yet variable time intervals on the prograde metamorphic path. This results in an underlying dispersion of the data set and potential disturbances that may arise from other inclusions are within this dispersion. Although zircon nucleated and grew in the matrix and was later overgrown by chloritoid, within the U–Pb date error it is valid to propose that zircon grew coevally with chloritoid, which formed at known *P–T* conditions. The zircon bulk inclusion age of the chloritoid rim is thus attributed to the late prograde evolution in the range of 460–485℃ and 0.5–0.7 GPa.

TABLE 3 Apparent ages from subsets of the chloritoid rim U–Pb data

Th/U subset	Age (Ma)	±2σ (Ma)	*n*	MSWD	Δ age (Ma)
<12	116.7	9.1	79	1.5	
<4	121.2	10.4	62	1.3	−4.5
<2	122.4	11.1	47	1.2	−5.7
<1.5	113.3	12.2	38	1.2	3.4

Our new *P–T* and age data are consistent with previously published data for the same nappe, although our *P–T* conditions indicate a higher metamorphic grade than the previous studies (Collins et al., 1980; Tropper & Piber, 2012). This is unsurprising, considering that our samples were collected at the base of the SHN, whereas the previously investigated samples come from higher structural positions. Late prograde metamorphism at 116.7 ± 9.1 Ma is consistent with published white mica K–Ar and $^{40}Ar/^{39}Ar$ ages from the same nappe (Frank & Schlager, 2006; Kralik, 1983). In contrast to conventional mica geochronology, the bulk inclusion U–Pb dating method allows a direct link to metamorphic *P–T* conditions. For the first time, we provide direct evidence that (a) peak metamorphism was reached relatively soon after sedimentation ceased at higher structural levels of the nappe at *c*. 125 Ma (Ortner et al., 2008) and (b) a relatively long period of *c*. 25–30 m.y. occurred between metamorphism in the upper structural level of the nappe stack and peak metamorphism of the eclogite-bearing units (*c*. 90 Ma; Thöni et al., 2008). This could imply that nappe stacking and metamorphism in low-grade units of the Austroalpine unit was a protracted process, which is in contrast to the postulated rapid exhumation of these eclogites (Thöni et al., 2008). This could alternatively reflect two different stages in the collision. Results of this study underscore the need of integrated *P–T–t–d* data for low-grade metamorphic rocks to better understand orogenic processes.

5.4 | Advantages and applicability of the bulk inclusion method

Metamorphic micro-zircon was documented in an Alpine chloritoid-bearing schist that experienced peak

metamorphism at 485℃ and 0.7 GPa. Although widely perceived as contaminants of the true trace element and isotopic composition of the porphyroblast (e.g. Scherer et al., 2000), we demonstrated that inclusions can be used to derive robust geochronological constraints of near-peak metamorphism in low-grade rocks and, potentially, the prograde evolution in higher grade rocks. The newly introduced method termed 'bulk inclusion' dating considerably improves the link of geochronological information and *P–T–d* data, which relies on well-established thermodynamic data of rock-forming minerals (e.g. Holland & Powell, 2011; White et al., 2014) rather than preliminary data from accessory minerals (Kelsey et al., 2008; Spear, 2010; Spear & Pyle, 2010). Once incorporated into porphyroblasts, small inclusions are shielded from fluids that may affect the otherwise closed system of accessory phases dated with conventional U–Pb geochronology (e.g. Grand'Homme et al., 2016), allowing rather straightforward interpretation. Bulk inclusion dating by LA-ICP-MS allows efficient and economical data acquisition avoiding the tedious task of precisely locating submicron-sized grains necessitated by high-resolution single grain analysis. With enhanced sensitivity of LA-ICP-MS instrumentation allowing analysis of smaller domains of porphyroblasts, the mass and spatial resolution of this method may significantly improve in future. Finally, we highlight the potential of the method for age determination of low-grade metamorphic rocks and emphasize their importance in the overall understanding of collisional orogeny.

ACKNOWLEDGEMENTS

This study was funded by the Uni:docs fellowship program of the University of Vienna and the Natural Sciences and Engineering Research Council of Canada. Finding the sample location would not have been possible without the work of Josef Aigner who mapped the area for his diploma thesis (1991, LMU Munich). We thank Brandon Boucher (UNB) for assistance with the U–Pb data acquisition. Ralf Schuster (GBA) is thanked for discussions about the regional geology and his comments on the manuscript. Discussions with Tom Griffiths, Anna Rogowitz, and Martin Schöpfer (all University of Vienna) on CSD and related statistics are greatly acknowledged. Finally, we want to thank editor Simon Harley, Tim Dempster, and an anonymous reviewer for their helpful comments that greatly improved the quality of the manuscript.

ORCID

M. Sophie Hollinetz https://orcid.org/0000-0001-8075-8847
David A. Schneider https://orcid.org/0000-0002-9665-4927
Benjamin Huet https://orcid.org/0000-0002-6591-4327
Gerd Rantitsch https://orcid.org/0000-0002-1101-1704
Bernhard Grasemann https://orcid.org/0000-0002-4647-8224

REFERENCES

Bergmann, R. B., & Bill, A. (2008). On the origin of logarithmic-normal distributions: An analytical derivation, and its application to nucleation and growth processes. *Journal of Crystal Growth*, *310*(13), 3135–3138. https://doi.org/10.1016/j.jcrysgro.2008.03.034

Bingen, B., Austrheim, H., & Whitehouse, M. (2001). Ilmenite as a source for zirconium during high-grade metamorphism? Textural evidence from the Caledonides of western Norway and implications for zircon geochronology. *Journal of Petrology*, *42*(2), 355–375. https://doi.org/10.1093/petrology/42.2.355

Cherniak, D. J. (2000). Pb diffusion in rutile. *Contributions to Mineralogy and Petrology*, *139*(2), 198–207. https://doi.org/10.1007/PL00007671

Cherniak, D. J. (2006). Zr diffusion in titanite. *Contributions to Mineralogy and Petrology*, *152*(5), 639–647. https://doi.org/10.1007/s00410-006-0133-0

Cherniak, D. J., & Watson, E. B. (2001). Pb diffusion in zircon. *Chemical Geology*, *172*(1–2), 5–24. https://doi.org/10.1016/S0009-2541(00)00233-3

Chew, D. M., Sylvester, P. J., & Tubrett, M. N. (2011). U-Pb and Th–Pb dating of apatite by LA-ICPMS. *Chemical Geology*, *280*(1–2), 200–216. https://doi.org/10.1016/j.chemgeo.2010.11.010

Coggon, R., & Holland, T. J. B. (2002). Mixing properties of phengitic micas and revised garnet-phengite thermobarometers. *Journal of Metamorphic Geology*, *20*(7), 683–696. https://doi.org/10.1046/j.1525-1314.2002.00395.x

Collins, E., Hoschek, G., & Mostler, H. (1980). Geologische Entwicklung und Metamorphose im Westabschnitt der nördlichen Grauwackenzone unter besonderer Berücksichtigung der Metabasite. *Mitteilungen Der Österreichischen Geologischen Gesellschaft*, *71*(72), 343–378.

Cossette, É., Schneider, D. A., Warren, C. J., & Grasemann, B. (2015). Lithological, rheological, and fluid infiltration control on $^{40}Ar/^{39}Ar$ ages in polydeformed rocks from the West Cycladic detachment system, Greece. *Lithosphere*, *7*(2), 189–205.

Darling, J. R., Storey, C. D., & Engi, M. (2012). Allanite U-Th–Pb geochronology by laser ablation ICPMS. *Chemical Geology*, *292*, 103–115. https://doi.org/10.1016/j.chemgeo.2011.11.012

Davis, J. C. (2003). *Statistics and Data Analysis in Geology* (3rd ed). Wiley, 656 p.

De Capitani, C., & Petrakakis, K. (2010). The computation of equilibrium assemblage diagrams with Theriak/Domino software. *American Mineralogist*, *95*(7), 1006–1016. https://doi.org/10.2138/am.2010.3354

Degeling, H., Eggins, S., & Ellis, D. J. (2001). Zr budgets for metamorphic reactions, and the formation of zircon from garnet breakdown. *Mineralogical Magazine*, *65*(6), 749–758. https://doi.org/10.1180/0026461016560006

Dempster, T. J., Hay, D. C., & Bluck, B. J. (2004). Zircon growth in slate. *Geology*, *32*(3), 221–224. https://doi.org/10.1130/G20156.1

Dempster, T. J., Hay, D. C., Gordon, S. H., & Kelly, N. M. (2008). Micro-zircon: Origin and evolution during metamorphism. *Journal of Metamorphic Geology*, *26*(5), 499–507. https://doi.org/10.1111/j.1525-1314.2008.00772.x

Didier, A., Bosse, V., Cherneva, Z., Gautier, P., Georgieva, M., Paquette, J. L., & Gerdjikov, I. (2014). Syn-deformation fluid-assisted growth of monazite during renewed high-grade metamorphism in metapelites of the Central Rhodope (Bulgaria, Greece). *Chemical Geology*, *381*, 206–222. https://doi.org/10.1016/j.chemgeo.2014.05.020

Eberlei, T., Habler, G., Wegner, W., Schuster, R., Körner, W., Thöni, M., & Abart, R. (2015). Rb/Sr isotopic and compositional retentivity of muscovite during deformation. *Lithos*, *227*, 161–178. https://doi.org/10.1016/j.lithos.2015.04.007

Engi, M. (2017). Petrochronology based on REE-minerals: Monazite, allanite, xenotime, apatite. *Reviews in Mineralogy and Geochemistry*, *83*(1), 365–418. https://doi.org/10.2138/rmg.2017.83.12

Ewing, R. C., Meldrum, A., Wang, L., Weber, W. J., & Corrales, L. R. (2003). Radiation effects in zircon. *Reviews in Mineralogy and Geochemistry*, *53*(1), 387–425. https://doi.org/10.2113/0530387

Frank, W., & Schlager, W. (2006). Jurassic strike slip versus subduction in the Eastern Alps. *International Journal of Earth Sciences*, *95*(3), 431–450. https://doi.org/10.1007/s00531-005-0045-7

Froitzheim, N., Plašienka, D., & Schuster, R. (2008). Alpine tectonics of the Alps and Western Carpathians. *The Geology of Central Europe*, *2*, 1141–1232.

Garver, J. I., & Kamp, P. J. (2002). Integration of zircon color and zircon fission-track zonation patterns in orogenic belts: Application to the Southern Alps, New Zealand. *Tectonophysics*, *349*(1–4), 203–219. https://doi.org/10.1016/S0040-1951(02)00054-9

Gieré, R., & Sorensen, S. S. (2004). Allanite and other REE-rich epidote-group minerals. *Reviews in Mineralogy and Geochemistry*, *56*(1), 431–493. https://doi.org/10.2138/gsrmg.56.1.431

Grand'Homme, A., Janots, E., Seydoux-Guillaume, A. M., Guillaume, D., Bosse, V., & Magnin, V. (2016). Partial resetting of the U-Th-Pb systems in experimentally altered monazite: Nanoscale evidence of incomplete replacement. *Geology*, *44*(6), 431–434. https://doi.org/10.1130/G37770.1

Harley, S. L., Kelly, N. M., & Möller, A. (2007). Zircon behaviour and the thermal histories of mountain chains. *Elements*, *3*(1), 25–30. https://doi.org/10.2113/gselements.3.1.25

Hay, D. C., & Dempster, T. J. (2009). Zircon behaviour during low-temperature metamorphism. *Journal of Petrology*, *50*(4), 571–589. https://doi.org/10.1093/petrology/egp011

Heaman, L. M., & LeCheminant, A. N. (1993). Paragenesis and U-Pb systematics of baddeleyite (ZrO_2). *Chemical Geology*, *110*(1–3), 95–126. https://doi.org/10.1016/0009-2541(93)90249-I

Heinisch, H., Pestal, G., & Reitner, J. (2015). Erläuterungen zu Blatt 122 Kitzbühel. 301 S., Geol. B. *A., Wien*.

Herwartz, D., Nagel, T. J., Münker, C., Scherer, E. E., & Froitzheim, N. (2011). Tracing two orogenic cycles in one eclogite sample by Lu–Hf garnet chronometry. *Nature Geoscience*, *4*(3), 178–183. https://doi.org/10.1038/ngeo1060

Higgins, M. D. (2000). Measurement of crystal size distributions. *American Mineralogist*, *85*(9), 1105–1116. https://doi.org/10.2138/am-2000-8-901

Holland, T. J. B., & Powell, R. (2011). An improved and extended internally consistent thermodynamic dataset for phases of petrological interest, involving a new equation of state for solids. *Journal of Metamorphic Geology*, *29*(3), 333–383. https://doi.org/10.1111/j.1525-1314.2010.00923.x

Horn, I., & Blanckenburg, F. (2007). Investigation on elemental and isotopic fractionation during 196 nm femtosecond laser ablation multiple collector inductively coupled plasma mass spectrometry. *Spectrochimica Acta Part B-Atomic Spectroscopy*, *62*(4), 410–422.

Janots, E., Engi, M., Berger, A., Allaz, J., Schwarz, J. O., & Spandler, C. (2008). Prograde metamorphic sequence of REE minerals in pelitic rocks of the Central Alps: Implications for allanite–monazite–xenotime phase relations from 250 to 610°C. *Journal of Metamorphic Geology*, *26*(5), 509–526.

Janots, E., Engi, M., Rubatto, D., Berger, A., Gregory, C., & Rahn, M. (2009). Metamorphic rates in collisional orogeny from in situ allanite and monazite dating. *Geology*, *37*(1), 11–14. https://doi.org/10.1130/G25192A.1

Janots, E., Negro, F., Brunet, F., Goffé, B., Engi, M., & Bouybaouene, M. L. (2006). Evolution of the REE mineralogy in HP–LT metapelites of the Sebtide complex, Rif, Morocco: Monazite stability and geochronology. *Lithos*, *87*(3–4), 214–234. https://doi.org/10.1016/j.lithos.2005.06.008

Kelly, C. J., Schneider, D. A., Jackson, S. E., Kalbfleisch, T., & McFarlane, C. R. (2017). Insights into low-to moderate-temperature recrystallization of zircon: Unpolished crystal depth profile techniques and geochemical mapping. *Chemical Geology*, *449*, 82–98. https://doi.org/10.1016/j.chemgeo.2016.11.035

Kelsey, D., Clark, C., & Hand, M. (2008). Thermobarometric modelling of zircon and monazite growth in melt-bearing systems: Examples using model metapelitic and metapsammitic granulites. *Journal of Metamorphic Geology*, *26*, 199–212. https://doi.org/10.1111/j.1525-1314.2007.00757.x

Ketcham, R. A. (2015). Calculation of stoichiometry from EMP data for apatite and other phases with mixing on monovalent anion sites. *American Mineralogist*, *100*(7), 1620–1623.

Kile, D. E., Eberl, D. D., Hoch, A. R., & Reddy, M. M. (2000). An assessment of calcite crystal growth mechanisms based on crystal size distributions. *Geochimica et Cosmochimica Acta*, *64*(17), 2937–2950. https://doi.org/10.1016/S0016-7037(00)00394-X

Kohn, M. J., Corrie, S. L., & Markley, C. (2015). The fall and rise of metamorphic zircon. *American Mineralogist*, *100*(4), 897–908. https://doi.org/10.2138/am-2015-5064

Kralik, M. (1983). Interpretation of K−Ar and Rb−Sr data from fine fractions of weakly metamorphosed shales and carbonate rocks at the base of the northern calcareous Alps (Salzburg, Austria). *Tschermaks Mineralogische Und Petrographische Mitteilungen*, *32*(1), 49–67. https://doi.org/10.1007/BF01081544

Kula, J., Spell, T. L., & Zanetti, K. A. (2010). $^{40}Ar/^{39}Ar$ analyses of artificially mixed micas and the treatment of complex age spectra from samples with multiple mica populations. *Chemical Geology*, *275*(1–2), 67–77. https://doi.org/10.1016/j.chemgeo.2010.04.015

Loeschke, J., & Heinisch, H. (1993). Palaeozoic volcanism of the Eastern Alps and its palaeotectonic significance. In J. F. von Raumer & F. Neubauer (Eds.), *Pre-Mesozoic geology in the Alps* (pp. 441–455). Springer.

Lünsdorf, N. K., Dunkl, I., Schmidt, B. C., Rantitsch, G., & von Eynatten, H. (2017). Towards a higher comparability of geothermometric data obtained by Raman spectroscopy of carbonaceous material. Part 2: A revised geothermometer. *Geostandards and Geoanalytical Research*, *41*, 593–661. https://doi.org/10.1111/ggr.12178

Lünsdorf, N. K., & Lünsdorf, J. O. (2016). Evaluating Raman spectra of carbonaceous matter by automated, iterative curve-fitting. *International Journal of Coal Geology*, *160*, 51–62.

Martin, L. A., Duchêne, S., Deloule, E., & Vanderhaeghe, O. (2008). Mobility of trace elements and oxygen in zircon during metamorphism: Consequences for geochemical tracing. *Earth and Planetary Science Letters*, *267*(1–2), 161–174. https://doi.org/10.1016/j.epsl.2007.11.029

McCarron, T. M., McFarlane, C. R. M., & Anczkiewicz, R. (2021). Recognizing juxtaposed metamorphic belts in the western Cape Breton Highlands, Nova Scotia through Lu-Hf garnet and U-Pb monazite, apatite and detrital zircon geochronology. *Journal of the Geological Society*, under review.

McFarlane, C. R. M., & Luo, Y. (2012). U-Pb geochronology using 193 nm Excimer LA-ICP-MS optimized for in situ accessory mineral dating in thin sections. *Geoscience Canada*, *39*, 158–172.

Murakami, T., Chakoumakos, B. C., Ewing, R. C., Lumpkin, G. R., & Weber, W. J. (1991). Alpha-decay event damage in zircon. *American Mineralogist*, *76*(9–10), 1510–1532.

Ntaflos, T., Bizimis, M., & Abart, R. (2017). Mantle xenoliths from Szentbékálla, Balaton: Geochemical and petrological constraints on the evolution of the lithospheric mantle underneath Pannonian Basin, Hungary. *Lithos*, *276*, 30–44. https://doi.org/10.1016/j.lithos.2016.12.018

Ortner, H., Ustaszewski, M., & Rittner, M. (2008). Late Jurassic tectonics and sedimentation: Breccias in the Unken syncline, central Northern Calcareous Alps. *Swiss Journal of Geosciences*, *101*(1), 55–71. https://doi.org/10.1007/s00015-008-1282-0

Paton, C., Hellstrom, J., Paul, B., Woodhead, J., & Hergt, J. (2011). Iolite: Freeware for the visualisation and processing of mass spectrometric data. *Journal of Analytical Atomic Spectrometry*, *26*, 2508–2518. https://doi.org/10.1039/c1ja10172b

Paton, C., Woodhead, J. D., Hellstrom, J. C., Hergt, J. M., Greig, A., & Maas, R. (2010). Improved laser ablation U-Pb zircon geochronology through robust downhole fractionation correction. *Geochemistry, Geophysics, Geosystems*, *11*(3). https://doi.org/10.1029/2009GC002618

Pestal, G., Hejl, E., & Braunstingl, R. (2005). Geologische Karte von Salzburg. *Geological Survey of Austria, Scale*, *1*, 200000.

Petrus, J. A., & Kamber, B. S. (2012). VizualAge: A novel approach to laser ablation ICP-MS UPb geochronology data reduction. *Geostandards and Geoanalytical Research*, *36*, 247–270. https://doi.org/10.1111/j.1751-908X.2012.00158.x

Phillips, N. J., & Williams, R. T. (2021). To D or not to D? Re-evaluating particle-size distributions in natural and experimental fault rocks. *Earth and Planetary Science Letters*, *553*, 116635. https://doi.org/10.1016/j.epsl.2020.116635

Plunder, A., Agard, P., Dubacq, B., Chopin, C., & Bellanger, M. (2012). How continuous and precise is the record of P-T paths? Insights from combined thermobarometry and thermodynamic modelling into subduction dynamics (Schistes Lustrés, W. Alps). *Journal of Metamorphic Geology*, *30*(3), 323–346. https://doi.org/10.1111/j.1525-1314.2011.00969.x

Powell, R., & Holland, T. J. B. (2008). On thermobarometry. *Journal of Metamorphic Geology*, *26*(2), 155–179. https://doi.org/10.1111/j.1525-1314.2007.00756.x

Rantitsch, G., & Judik, K. (2009). Alpine metamorphism in the central segment of the Western Greywacke Zone (Eastern Alps). *Geologica Carpathica*, *60*(4), 319–329. https://doi.org/10.2478/v10096-009-0023-2

Rasmussen, B. (2005). Zircon growth in very low grade metasedimentary rocks: Evidence for zirconium mobility at ~250°C. *Contributions to Mineralogy and Petrology*, *150*(2), 146–155. https://doi.org/10.1007/s00410-005-0006-y

Ribeiro, B. V., Lagoeiro, L., Faleiros, F. M., Hunter, N., Queiroga, G., Raveggi, M., Cawood, P. A., Finch, M., & Campanha, G. (2020). Strain localization and fluid-assisted deformation in apatite and its influence on trace elements and U-Pb systematics. *Earth and Planetary Science Letters*, *545*, 116421. https://doi.org/10.1016/j.epsl.2020.116421

Rubatto, D. (2002). Zircon trace element geochemistry: Partitioning with garnet and the link between U-Pb ages and metamorphism. *Chemical Geology*, *184*(1–2), 123–138. https://doi.org/10.1016/S0009-2541(01)00355-2

Rubatto, D. (2017). Zircon: The metamorphic mineral. *Reviews in Mineralogy and Geochemistry*, *83*(1), 261–295. https://doi.org/10.2138/rmg.2017.83.9

Rudnick, R. L., Gao, S., Holland, H. D., & Turekian, K. K. (2003). Composition of the continental crust. *The Crust*, *3*, 1–64.

Scherer, E. E., Cameron, K. L., & Blichert-Toft, J. (2000). Lu–Hf garnet geochronology: Closure temperature relative to the Sm–Nd system and the effects of trace mineral inclusions. *Geochimica et Cosmochimica Acta*, *64*(19), 3413–3432. https://doi.org/10.1016/S0016-7037(00)00440-3

Schindelin, J., Arganda-Carreras, I., Frise, E., Kaynig, V., Longair, M., Pietzsch, T., Preibisch, S., Rueden, C., Saalfeld, S., Schmid, B., Tinevez, J.-Y., White, D. J., Hartenstein, V., Eliceiri, K., Tomancak, P., & Cardona, A. (2012). Fiji: An open-source platform for biological-image analysis. *Nature Methods*, *9*(7), 676–682. https://doi.org/10.1038/nmeth.2019

Schmid, S., Fügenschuh, B., Kissling, E., & Schuster, R. (2004). Tectonic map and overall architecture of the Alpine orogen. *Eclogae Geologicae Helvetiae*, *97*, 93–117. https://doi.org/10.1007/s00015-004-1113-x

Shimizu, I. (1999). A stochastic model of grain size distribution during dynamic recrystallization. *Philosophical Magazine A*, *79*(5), 1217–1231. https://doi.org/10.1080/01418619908210357

Sölva, H., Grasemann, B., Thöni, M., Thiede, R., & Habler, G. (2005). The Schneeberg normal fault zone: Normal faulting associated with Cretaceous SE-directed extrusion in the Eastern Alps (Italy/Austria). *Tectonophysics*, *401*(3–4), 143–166. https://doi.org/10.1016/j.tecto.2005.02.005

Spear, F. S. (2010). Monazite–allanite phase relations in metapelites. *Chemical Geology*, *279*(1–2), 55–62. https://doi.org/10.1016/j.chemgeo.2010.10.004

Spear, F. S., & Pyle, J. M. (2010). Theoretical modeling of monazite growth in a low-Ca metapelite. *Chemical Geology*, *273*(1–2), 111–119. https://doi.org/10.1016/j.chemgeo.2010.02.016

Stacey, J. T., & Kramers, J. D. (1975). Approximation of terrestrial lead isotope evolution by a two-stage model. *Earth and Planetary Science Letters*, *26*(2), 207–221. https://doi.org/10.1016/0012-821X(75)90088-6

Szpak, Z. L., Chojnacki, W., Eriksson, A., & van den Hengel, A. (2014). Sampson distance based joint estimation of multiple homographies with uncalibrated cameras. *Computer Vision and Image Understanding*, *125*, 200–213. https://doi.org/10.1016/j.cviu.2014.04.008

Tenczer, V., & Stüwe, K. (2003). The metamorphic field gradient in the eclogite type locality, Koralpe region, Eastern Alps. *Journal of Metamorphic Geology*, *21*(4), 377–393. https://doi.org/10.1046/j.1525-1314.2003.00448.x

Thöni, M. (2006). Dating eclogite-facies metamorphism in the Eastern Alps–approaches, results, interpretations: A review. *Mineralogy and Petrology*, *88*(1–2), 123–148. https://doi.org/10.1007/s00710-006-0153-5

Thöni, M., Miller, C., Blichert-Toft, J., Whitehouse, M. J., Konzett, J., & Zanetti, A. (2008). Timing of high-pressure metamorphism and exhumation of the eclogite type-locality (Kupplerbrunn–Prickler Halt, Saualpe, south-eastern Austria): Constraints from correlations of the Sm–Nd, Lu–Hf, U-Pb and Rb–Sr isotopic systems. *Journal of Metamorphic Geology*, *26*(5), 561–581. https://doi.org/10.1111/j.1525-1314.2008.00778.x

Tropper, P., & Piber, A. (2012). Geothermobarometry of quartzphyllites, orthogneisses and greenschists of the Austroalpine Basement

Nappes in the northern Zillertal (Innsbruck Quartzphyllite Complex, Kellerjochgneis, Wild-schönau Schists; Tyrol, Eastern Alps). *Austrian Journal of Earth Sciences*, *105*(3), 80–94.

Ventura, G. D., Bellatreccia, F., & Williams, C. T. (1999). Zr-and LREE-rich titanite from Tre Croci, Vico volcanic complex (Latium, Italy). *Mineralogical Magazine*, *63*(1), 123–130.

Vermeesch, P. (2018). IsoplotR: A free and open toolbox for geochronology. *Geoscience Frontiers*, *9*(5), 1479–1493. https://doi.org/10.1016/j.gsf.2018.04.001

Watson, E. B., Chemiak, D. J., Hanchar, J. M., Harrison, T. M., & Wark, D. A. (1997). The incorporation of Pb into zircon. *Chemical Geology*, *141*(1–2), 19–31. https://doi.org/10.1016/S0009-2541(97)00054-5

White, R. W., Powell, R., & Johnson, T. E. (2014). The effect of Mn on mineral stability in metapelites revisited: New a–x relations for manganese-bearing minerals. *Journal of Metamorphic Geology*, *32*(8), 809–828.

Whitney, D. L., & Evans, B. W. (2010). Abbreviations for names of rock-forming minerals. *American Mineralogist*, *95*(1), 185–187. https://doi.org/10.2138/am.2010.3371

Yakymchuk, C., Kirkland, C. L., & Clark, C. (2018). Th/U ratios in metamorphic zircon. *Journal of Metamorphic Geology*, *36*(6), 715–737. https://doi.org/10.1111/jmg.12307

SUPPORTING INFORMATION

Additional supporting information may be found online in the Supporting Information section.

Appendix S1. Whole-rock analyses and model bulk rock composition.

Appendix S2. Modifications of the thermodynamic database.

Appendix S3. Contribution of apatite to the bulk inclusion U concentration.

Table S1. EPMA data of chloritoid, chlorite, garnet, ilmenite, hematite, white mica, and rutile from samples A and B.

Table S2. Full EPMA data set of apatite from sample A.

Table S3. Results of RSCM thermometry.

Table S4. Zircon crystal size data.

Table S5. Results of bulk inclusion trace element LA-ICP-MS analysis from sample A.

Table S6. Results of apatite U–Pb LA-ICP-MS analysis from sample A.

Table S7. Results of chloritoid rim bulk inclusion U–Pb LA-ICP-MS analysis from sample A.

How to cite this article: Hollinetz, M. S., Schneider, D. A., McFarlane, C. R. M., Huet, B., Rantitsch, G., & Grasemann, B. (2021). Bulk inclusion micro-zircon U–Pb geochronology: A new tool to date low-grade metamorphism. *Journal of Metamorphic Geology*, 00, 1–21. https://doi.org/10.1111/jmg.12624